August 2019

Sensing with Geometry-Dependent Magnetostriction Via an Embedded Fiber Bragg Grating

David Frailey
University of Wisconsin-Milwaukee

SENSING WITH GEOMETRY-DEPENDENT MAGNETOSTRICTION VIA AN EMBEDDED FIBER BRAGG GRATING

by

David Frailey

A Thesis Submitted in

Partial Fulfillment of the

Requirements for the Degree of

Master of Science

in Engineering

at

The University of Wisconsin-Milwaukee

August 2019

ABSTRACT

SENSING WITH GEOMETRY-DEPENDENT MAGNETOSTRICTION VIA AN EMBEDDED FIBER BRAGG GRATING

by

David Frailey

The University of Wisconsin-Milwaukee, 2019
Under the Supervision of Professor Chiu Tai Law

Fiber optic current sensors (FOCSs) have unique advantages in electromagnetic interference immunity and direct current measurements. Here, magnetostrictive composites and their interactions with embedded fiber Bragg gratings (FBG) were explored to form novel FOCSs with predictable and temperature-independent sensitivity. Magnetostrictive, particularly Terfenol-D/epoxy, composites maintain the mangetostrictive expansion under an external magnetic field while gaining flexibility in engineering. In contrast to ordinary strain gauges, an embedded FBG can provide an optical signal inferring simultaneously a strain and its gradient inside a composite. In principle, the sensing of strain gradient is thermally independent. Creating appropriate geometries for magnetostrictive composites enables the conversion of a uniform external magnetic field into an internal one with a certain field gradient that enacts a strain distribution inside the composite transferred to the FBG. Hence, the strain gradient sensing with the FBG can be exploited for temperature independent measurement of the external magnetic field. Such a strain gradient will alter the spectral properties of the FBG, such as the power and bandwidth of the returned optical signal. The experimental results from two separate sensors have confirmed the trend that is predicted by the theory and simulations. They will substantiate the claim of sensitivity tuning solely

with geometry. These FOCSs will provide reliable reading for wide operating temperatures if the underlying materials allow.

TABLE OF CONTENTS

LIST OF FIGURES

ACKNOWLEDGEMENTS

First, a thank you to my advisor Dr. Chiu Law. It has been an honor to be able to have you as my advisor. From the courses that you have taught me, to working on this thesis, I truly appreciate everything you have done for me. I look forward to PhD studies with you as my continuing advisor.

I would also like to thank Dr. George Hanson. While the study of electromagnetics is one of the most difficult challenges among the electrical engineering community, it was a pleasure to take all the classes I have taken with you since I started graduate school.

Thank you, Dr. Rani El-Hajjar for not only providing much of the equipment that I used in the lab, but also the advice you have given me.

Thank you to my labmates, Esteban Jimenez and Nathan Swanson. From collaborating on projects, to regular conversations, I enjoyed every moment of working in the lab together. I look forward to engaging in future projects with the both of you.

Lastly, I would like to thank the people that made me a better person throughout my current journey of electrical engineering: Ana Tomaich, Casey Marnocha, Devon Zarcone, Gabe Merriman, Sabrina Wolf, Rob Koltz, and Ivan Lopez. I wish you all nothing but the best in life.

Chapter 1

Introduction

1.1 Background on Optical Current Sensors and Fiber Bragg Gratings

The ubiquitous influence of the power grid is obvious. The blackout on August 14, 2003 that caused major power outage in large areas of the northeastern United States and Canada highlights the vulnerability of the intricate power transmission system. It is absolutely impossible to overlook the astronomical cost of an outage. For examples, the August 14, 2003 blackout impacted 50 million people and its economic loss was estimated to be between $6 and $10 billion. To address that, companies, such as ABB and Rockwell Automation, have actively researched and developed solutions for power system protection. Key components for these solutions are sensors that can detect anomalies in a power system. Optical sensors are unique in terms of their immunity from electromagnetic interference (EMI). Hence, they are excellent candidates to operate at high voltage and current environment. Recently, a research group at ABB has integrated a fiber optical current sensor (FOCS) with a 420 kV circuit breaker [1]. The applications of optical sensors for power distribution systems have been proposed [2], [3]. Currently, the proliferation of connected systems and Internet of things, including smart grids, will requires more sensors but at various voltage and current levels.

Optical current sensors can be grouped into four main categories. The first category uses

an optical fiber as the sensing element, which may consist of single-mode, multi-mode, or Bragg grating fibers. The second method involves a bulk glass to sense a current. The third employs an electro-optic hybrid method where optical energy and electrical energy are converted back and forth as needed. This method is good for retrofitting optical sensor to existing infrastructure but has slow response. Lastly, optical current sensors are based on certain physical process in coupling magnetic field to optical properties of devices. This can be done with the Faraday effect to change the polarization of the measured light, or through an optical sensor interfacing with a magnetostrictive transducer [4].

Fiber-based sensors are useful in applications where traditional transducers are subjected to strong EMI. Additionally, they are much lighter in weight, take up less space, and use less material. Corrosion does not occur within the fiber since it is made of silica. Further more, this allows for the material to be more sustainable than common transducers. Faraday-effect-based FOCS requires polarization maintaining fibers and elaborate scheme to mitigate various environmental disturbances while detecting changes within a limited range of polarization angle [5]. On the other hand, magnetostriction-based FOCS has been shown to have more pronounced effect [6]. The magnetostrictive transducer can be interfaced with a fiber Bragg grating (FBG) [7] - [12]. or an optical fiber extrinsic Fabry-Perot interferometric (EFPI) [13], [14]. FOCSs with EFPI have higher sensitivity but more complicated device structures. FOCSs with FBG usually are simpler in construction and easily to form a sensor network that can be readily integrated with an optical fiber communication system. This thesis discusses the modeling and fabrication of magnetostriction-based FOCSs with FBG. Thermal drift is a common problem for the sensor design. For thermal compensation, various groups [7], [8], [9] have used non-magnetostrictive materials with almost the same thermal expansion coefficient as their magnetostrictive counterparts, such as the use of MONEL 400 as a thermal compensator for Terfenol-D. By replacing the cladding of an FBG with a Terfenol-D thin film, the sensitivity of a magnetostriction-based FOCS can be enhanced [11].

Fault detection of power distribution systems have conceptually utilized sensor network with

Terfenol-D-based FOCSs [3] that replace conventional current transformers or potential transformers in breakers and reclosers. With the speed of the propagating light, real time measurements are able to be performed which do not depend on past events. Another advantage of this sensor network is the absence of both saturation and hysteresis of the current transformers during large current faults. To further extend the operating frequency of a magnetostriction-based FOCS, Terfenol-D composite can be used [12]. However, the use of Terfenol-D composite reduced the size of magnetostriction, i.e. the sensitivity of sensors. For applications with systems at various voltage levels, an effective means for control and enhancement of sensitivity becomes necessary. New opportunities for achieving these goals and thermal independent sensing arise when the operation of an FBG is revisited. An FBG is a periodic modulation of the refractive index along the core of an optical fiber. Depending on the grating (modulation) period and uniformity of the refractive indices, different effects can be seen in terms of reflectance and transmittance. By applying a strain on the FBG axis, these optical properties can be altered. The strain applied to the FBG can be due to an external magnetic field, thermal expansion, and external stress [15]. Small differences in grating period caused by the strain on the FBG can create large differences in the output of the FBG in both the reflected spectrum and reflected optical power since both wavelength and bandwidth are sensitive to strain and its distribution. In fact, it has been shown that changes in bandwidth can be decoupled from those in the length for the FBG so that a sensor can be designed for detection of both stress and temperature [15]. This unique property of the FBG as a strain gauge is caused by the frequency chirping associated with the strain distribution. Similarly, attaching the FBG to a composite slab in certain shape that can be geometrically deformed differently under various level of external magnetic fields enables the design of a temperature independent FOCS. Particularly, the geometry of the slab is a key design consideration for enhancing sensor sensitivity.

1.2 Thesis Objectives

This thesis will demonstrate the sensing of magnetic field with an FBG coupled to a magnetostrictive composite. As mentioned in the previous section, the use of composite enables fast detection of magnetic field while the geometry of the composite slab determines the sensor sensitivity. FOCSs under consideration are based on the formation of chirped FBGs induced by strain distribution along its axis. Such a sensing principle is inherently not affected by temperature and enables the inference of the magnetic field in terms of optical power. Particularly, a Terfenol-D/epoxy composite slab is fabricated with an embedded FBG. Terfenol-D exhibits a very large magnetostriction effect which will result in a strain along the longitudinal axis of the Terfenol-D/epoxy composite slab. The geometry of the slab dictates the demagnetization field inside the slab in reaction to an external magnetic field. As a result, the internal magnetic field is reduced and varies along the FBG axis establishing a strain distribution. Theoretical model for the internal magnetic field will be calculated analytically and numerically. Since the use of Terfenol-D/epoxy facilitates the shaping of the slab into an arbitrary geometry, two particular shapes (trapezoid and approximately acute Saccheri quadrilateral) of the slab are investigated. With a non-rectangular slab composite, a non-uniform magnetic field is created and resulted in a non-uniform magnetostriction effect. Owing to a non-uniform magnetostriction, the FBG encounters different strains at different points along the longitudinal axis as the FBG is directly bonded to the composite during the curing process. During FOCS characterization, reflection spectra and power are recorded for each magnetic field level. These transfer characteristics will be used to corroborate with the theory. The comparison between results for trapezoid and approximately acute Saccheri quadrilateral will demonstrate the control of sensitivity via slab geometry. Through these modeling and experimenting processes, the understanding of the FOCS theory, fabrication and physics will be enriched and refined.

1.3 Thesis Structure

Chapter 2 will include the origin of magnetostriction and how it applies to magnetic bodies. Terfenol-D will be introduced and the properties such as strain will be shown. Additional comparisons between bulk material monolithic Terfenol-D and Terfenol-D/epoxy composites will be examined.

Chapter 3 will introduce the concept of an FBG and its optical properties.

Chapter 4 will cover the theoretical analysis of the experiment. This will consist of the derivation of the magnetization of a magnetic body. The modeling of an FBG without strain will be simulated first. Next, an FBG with non-uniform strain will be evaluated. The non-uniform strain can be modeled from the magnetization of the body and relating that to the magnetostrictive effect. From this non-uniform strain, the power reflected by the FBG can also be calculated. Finally, the theoretical results will be discussed with implications for sensor implementations.

Chapter 5 will discuss the experimental setup. This will entail the process of making the magnetostrictive composite, along with its attachment to an FBG. Additional details of the experiment will also be discussed if the experiment is desired to be reproduced by others, or as an aid for considering different geometries. Also, the experimental procedure and results will be shown, and compared to the theoretical results.

Chapter 6 will summarize and state the implication of experimental results collected during the thesis research period. Additionally, future work that may be interesting to pursue for further optimization and other application beyond sensing will be elucidated.

THIS PAGE INTENTIONALLY LEFT BLANK

Chapter 2

Magnetostriction

2.1 Introduction

For certain materials, when there is a change in their magnetization, a geometrical deformation can occur which is classified as a magnetostrictive effect. This change in the magnetization (magnetic moment per unit volume) is present when the material is placed in a magnetic field. Magnetostriction occurs to an extent for all magnetic materials. There are two distinguished situations that magnetostriction provides. The first being a linear deformation proportional to an increase in field intensity. The second being a rotational deformation due to the changing direction of a constant field. Giant magnetostriction only occurs in few materials with rare earth elements, such as Terfenol-D [16]. Magnetic moments of electrons dictate the metallic properties of a material. When these magnetic moments do not have a net-zero balancing, magnetism is achieved. When this imbalance is present, the electrons can order in a way where the net magnetic moment is in a particular direction, thus, lowering the crystal symmetry and producing new properties such as magnetostriction. [16]

Classically, if one considers an atom with an electron orbiting around a nucleus, the electron can be thought of as a current. From this interpretation, the Biot-Savart law can be used to calculate the magnetic moment. Quantum mechanically, electrons carry an intrinsic

property known as spin which is also a contributing component to the complete magnetic moment. If every orbit of an atom is considered where n_+ is the number of orbitals with a positive spin (+) and n_- is the number of orbitals with a negative spin (−), then the net spin moment (μ_s) for an atom can be given by

$$\mu_S = \mu_B(n_+ - n_-), \tag{2.1}$$

where μ_B is the magnetic moment of a single electron spin [16]. For rare earth elements, the inner orbital shell consists of unbalanced spins which do not interact with immediate atoms in the solid. This imbalance creates μ_S to be large from Eq. (2.1). The total magnetic moment is the sum of the effects from the orbital and spin. Strong magnetic moments are present in atoms that have an anisotropic charge cloud density. This characteristic is due to coupling with the spin property of the electron and partially filled shells.

Another property must be considered when analyzing magnetostriction; this is magneto-elastic coupling. This is defined as the interaction between the magnetization and the strain of a magnetic material. When a magnetic material is placed in a magnetic field, the field will force the magnetic moment to align as parallel as possible to the applied field. This can happen in two ways. The first way is the rotation of the magnetization vector to align with the field. The second is the expansion of molecular domains along the direction of the applied field [16]. When the magnetization vector is completely parallel with the field, saturation occurs.

2.1.1 Stoner-Wohlfarth Model

The Stoner-Wohlfarth model describes the physical phenomenon of atomic sized grains consisting of single sized magnetic domains. If a ferromagnetic material is considered with a magnetic field applied to it, there is a change in the magnetization. Consider Figure

2-1, where a magnetic domain is oriented at some angle θ from the x-axis, and an external magnetic field is at some angle ϕ from the x-axis. The Stoner-Wohlfarth model has the magnetic domain in these two potentials (magnetic energy induced by the charge cloud and the external magnetic field).

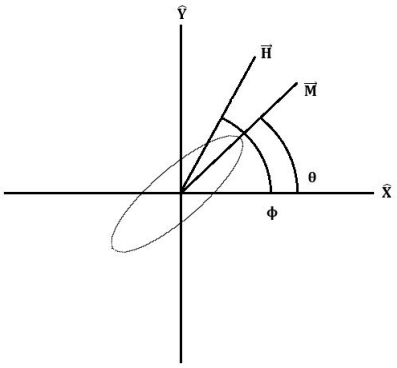

Figure 2-1: Magnetic Domain

Since only a single domain is considered, any effects from neighboring atoms have been ignored. The total energy (E_{tot}) for the system can be expressed as

$$E_{tot} = E_A + E_H, \tag{2.2}$$

where the anisotropic energy (E_A) can be thought of as a potential energy from the anisotropy from the domain. The energy from the external field can be defined as

$$E_H = -\vec{M} \cdot \vec{H}, \tag{2.3}$$

where $\vec{M}$ is the magnetization vector and $\vec{H}$ is the applied magnetic field intensity. The anisotropic energy can be written in terms of relative position of the magnetization vector with respect to the easy axis [17].

$$E_A = K \sin^2(\theta). \tag{2.4}$$

K is a constant associated with the magnetic anisotropy energy. Rewriting Eq. (2.2) results in

$$E_{tot} = K\sin^2(\theta) - \vec{M}\cdot\vec{H} = K\sin^2(\theta) - |\vec{M}||\vec{H}|\cos(\theta-\phi), \tag{2.5}$$

where $|\vec{M}|$ can be written as the saturation value of the magnetization ($|M_s|$). Since the magnetic moment will desire to have the lowest energy, the derivative with respect to θ can be taken for Eq. (2.5). Thus,

$$\frac{d}{d\theta}E_{tot} = 2K\sin(\theta)\cos(\theta) + M_s|\vec{H}|\sin(\theta-\phi) = 0. \tag{2.6}$$

Also, the second derivative must be taken to assure a concave up shape to guarantee it is a minimum.

$$\frac{d^2}{d^2\theta}E_{tot} = 2K\cos(2\theta) + M_s|\vec{H}|\cos(\theta-\phi) > 0. \tag{2.7}$$

Given the parameters of the magnitude and orientation of the external field, θ can be found for minimum energy. Implementing the normalization constant $h = \frac{M_s|\vec{H}|}{2K}$, Eq. (2.5) can be written as

$$E_{tot} = \sin^2(\theta) - 2h\cos(\theta-\phi). \tag{2.8}$$

The Stoner-Wohlfarth model is useful for representing individual atoms as magnetic domains. Due to this, the demagnetization component can be ignored. By varying the angle of the applied field, vastly different results can occur. Consider $\phi = 0$.

$$E_{tot} = \sin^2(\theta) - 2h\cos(\theta), \tag{2.9}$$

$$\frac{d}{d\theta}E_{tot} = 2K\sin(\theta)\cos(\theta) + M_s|\vec{H}|\sin(\theta) = 0. \tag{2.10}$$

θ can be analytically solved,

$$\theta = \cos^{-1}\left(\frac{-M_s|\vec{H}|}{2K}\right) = cos^{-1}(-h). \tag{2.11}$$

This imposes the conditions for $h\ \epsilon[-1,1]$ for solely real angles to be solutions. From this, the saturation for the external field can be expressed as

$$|\vec{H}| = \frac{2K}{M_s}. \tag{2.12}$$

Now considering the external field perpendicular to the easy-axis such that $\phi = \pi/2$,

$$E_{tot} = K\sin^2(\theta) - |\vec{M}||\vec{H}|\cos(\theta - \pi/2). \tag{2.13}$$

Taking the derivative to find the angle to minimize energy

$$\theta = \sin^{-1}(h), \tag{2.14}$$

and the concavity parameters follows

$$\cos^2(\theta) > 0. \tag{2.15}$$

It is common that $\vec{M}$ is expressed along the parallel ($\vec{p}$) and orthogonal ($\vec{o}$) components with respect to the magnetic field direction

$$\vec{M}_p = M_s\cos(\theta - \phi)\vec{p}, \tag{2.16}$$

$$\vec{M}_o = M_s\sin(\theta - \phi)\vec{o}. \tag{2.17}$$

For $\phi = 0$, the solutions of $\theta = n\pi$ for $n = 0, 1, 2\ldots$

Such that

$$\vec{M}_p = M_s\vec{p}, \tag{2.18}$$

$$\vec{M}_o = 0\vec{o}. \tag{2.19}$$

For $\phi = \pi/2$, the solutions of $\theta = \sin^{-1}(h)$ are

$$\vec{M}_p = M_s h \vec{p}. \tag{2.20}$$

$$\vec{M}_o = M_s \sqrt{1 - h^2} \vec{o}. \tag{2.21}$$

When the field is applied along the non-easy-axis, the magnetization vector becomes a function of h and has both parallel and orthogonal contributions when compared to the field on the easy-axis.

2.1.2 Magneto-Elastic Energy

When the magnetic domain is forced into position from an external magnetic field, an additional interaction must be accounted for which is the potential energy associated with the magnetic anisotropy and the electronic distribution of the material that will strain due to the alignment of the domains. The first is related to the direction that the domain will be in when relaxed, and the second is associated with the elastic response. This results in the elongation in a certain direction due to the domain rotation. To evaluate the magneto-elastic energy, the elastic energy must first be considered. This elastic energy(E_{elas}) is due to the deformation of the object which can be given by Eq. (2.22) [16]. C_{ij} $(i, j = 1, 2)$ are constants and ξ_{nm} $(n, m = x, y)$ are the elements of the strain tensor.

$$E_{elas} = \frac{1}{2} C_{11} \xi_{xx}^2 + \frac{1}{2} C_{11} \xi_{yy}^2 + C_{11} \xi_{xx}^2 \xi_{yy}^2 + \frac{1}{2} \left(\frac{C_{11} - C_{12}}{2} \right) \xi_{xy}^2 \tag{2.22}$$

Now when writing the total energy equation,

$$E_{tot} = E_A + E_H + E_{elas} + E_{me} \tag{2.23}$$

where E_{me} is the magnetoelastic coupling which can be defined as

$$E_{me} = b\left(\xi_{xx}^2\left[\frac{M_x}{M_s}\right]^2 + \xi_{yy}^2\left[\frac{M_x}{M_s}\right]^2 + \xi_{xy}^2\frac{M_xM_y}{M_s^2}\right), \tag{2.24}$$

where b is the coupling factor. If the material is anisotropic,

$$E_{me} = b_{xx}\xi_{xx}^2\left[\frac{M_x}{M_s}\right]^2 + b_{yy}\xi_{yy}^2\left[\frac{M_x}{M_s}\right]^2 + b_{xy}\xi_{xy}^2\frac{M_xM_y}{M_s^2}. \tag{2.25}$$

Noting that $\sin(\theta) = \frac{M_y}{M_s}$ and $\cos(\theta) = \frac{M_x}{M_s}$, Eq. (2.24) can be rewritten as

$$E_{me} = b\left(\xi_{xx}^2\cos^2(\theta) + \xi_{yy}^2\sin^2(\theta) + \xi_{xy}^2\cos(\theta)\sin(\theta)\right). \tag{2.26}$$

Thus, the total energy equation can be expanded as

$$\begin{aligned} E_{tot} =& K\sin^2(\theta) - HM_s\cos(\theta-\phi) + \frac{1}{2}C_{11}\xi_{xx}^2 \\ &+ \frac{1}{2}C_{11}\xi_{yy}^2 + C_{11}\xi_{xx}^2\xi_{yy}^2 + \frac{1}{2}\left(\frac{C_{11}-C_{12}}{2}\right)\xi_{xy}^2 \\ &+ b\left(\xi_{xx}^2\cos^2(\theta) + \xi_{yy}^2\sin^2(\theta) + \xi_{xy}^2\cos(\theta)\sin(\theta)\right). \end{aligned} \tag{2.27}$$

Minimizing conditions can be found by taking the derivative with respect to θ and ξ_{nm} which will allow to relate the magneto-elastic coupling energy with the elastic energy.

$$C_{11}\xi_{xx} + C_{12}\xi_{yy} = b\cos^2(\theta) \tag{2.28}$$

$$C_{11}\xi_{yy} + C_{12}\xi_{xx} = b\sin^2(\theta) \tag{2.29}$$

$$\left(\frac{C_{11}-C_{12}}{2}\right)\xi_{xy} = b\sin(\theta)\cos(\theta) \tag{2.30}$$

The magnetostriction constant is defined by the change in the strain ξ_{nm} when the magnetization vector is at 0 to 90° [18].The previous two equations simplify to

$$\xi_{yy} = \frac{bC_{11}}{C_{11}^2 - C_{12}^2}, \tag{2.31}$$

$$\xi_{xx} = \frac{-bC_{12}}{C_{11}^2 - C_{12}^2}. \tag{2.32}$$

The magnetostriction coefficient can be taken by the difference in strain from θ going from 0 to 90°. The resulting magnetostriction coefficients are

$$\Delta\xi_{yy} = \frac{b}{C_{12} - C_{11}}, \tag{2.33}$$

$$\Delta\xi_{xx} = \frac{b}{C_{12} - C_{11}}. \tag{2.34}$$

Since the assumption of the elastic energy and magneto-elastic energy have been set to be isotropic, the coefficients result to be the same. The general magnetostriction coefficient can be expressed as

$$\Delta\xi_{ii} = \frac{b}{C_{12} - C_{11}}. \tag{2.35}$$

2.2 Terfenol-D

Terfenol-D is an alloy material and exhibits the highest magnetostriction of all alloys. It was developed in the 1960's for military applications and is currently used in transducers at frequencies up to 20 kHz. It is comprised of Terbium, Dysprosium, and Iron ($Tb_xDy_{1-x}Fe_2$). For this thesis, the magnetostrictive samples were Terfenol-D/epoxy composites with an unloaded prestress.

By integrating Terfenol-D particles into a non-metallic binder, the electrical resistivity of the sample increases which in turn, reduces the eddy current losses and reduces the heat generation [20]. It can be inferred that because of this composite, the total deformation is less than a pure sample of Terfenol-D but will recover monolithic properties well.

2.2.1 Strain Properties of Terfenol-D

For magnetostrictive materials, the strain dependence on the magnetization for randomly oriented dipoles can be expressed as

$$\epsilon(M(\mathbf{r}')) = \frac{3}{2}\epsilon_s \left(\frac{M^2(\mathbf{r}')}{M_s^2} \right) \tag{2.36}$$

where $\mathbf{r}'$ is the spatial coordinates inside the material. ϵ_s is the magnetostriction coefficient that was derived in Eq. (2.35), and M_s is the saturation magnetization. For monolithic Terfenol-D, $\epsilon_s = 2000$[ppm] and $M_s = 1.6 \times 10^6$[A/m] [18].

2.2.2 Terfenol-D Resin Compound

While a monolithic sample of Terfenol-D would produce a very large magnetostriction under a magnetic field, it is difficult to shape pure samples into different geometries. Having an epoxy binder enables better formability. Recall that for each magnetic dipole of the bulk material for random orientation, the applied external field creates a shift in the dipole and this chain reaction causes the elongation. Terfenol-D powder consists of particles sis size of 100-300[μm]. Each particle can be thought of as a localized magnetic domain in the epoxy binder. Previous research on particle distribution for Terfenol-D/epoxy composites suggest that larger sized particles (100 to 300 [μm]) produced larger magnetostrictive strains compared to smaller particles (<100[μm]) which were preferred in applications for compressive strengths [19]. The composite is then placed in a magnetic field when curing to align the domain with the field. The aligned particles then form pillars due to the alignment of the magnetic domains along the flux lines. When relaxed from the curing magnetic field, the individual magnetic dipole for each atom in the particle domain will relax to a position away from the previously aligned magnetic field. These pillars simulate bulk material Terfenol-D with a magnetostriction coefficient and properties that are appropriately similar to original bulk material [16], [20], [21]. From [20], the optimal volume fraction of Terfenol-D powder was 30% which resulted in a magnetostriction coefficient of approximately half of the

monolithic Terfenol-D sample. The use of resins could shift the optimal volume ratio to be near 60% [20].

Additionally, studies with continuous fibers of Terfenol-D have had their magnetostrictive characteristics examined and have shown to be significantly closer to monolithic Terfenol-D [18]. A cost advantage supports the use of aligned particles compared to the continuous fiber chains. Experimentally, with the resin used in this experiment, a volume ratio of 33% was found to be optimal. The sample has recovered a fair amount of monolithic magnetostrictive properties, but is also very malleable to be formed to complex geometries. Figure 2-2 shows the aligned pillars from the samples created for this research.

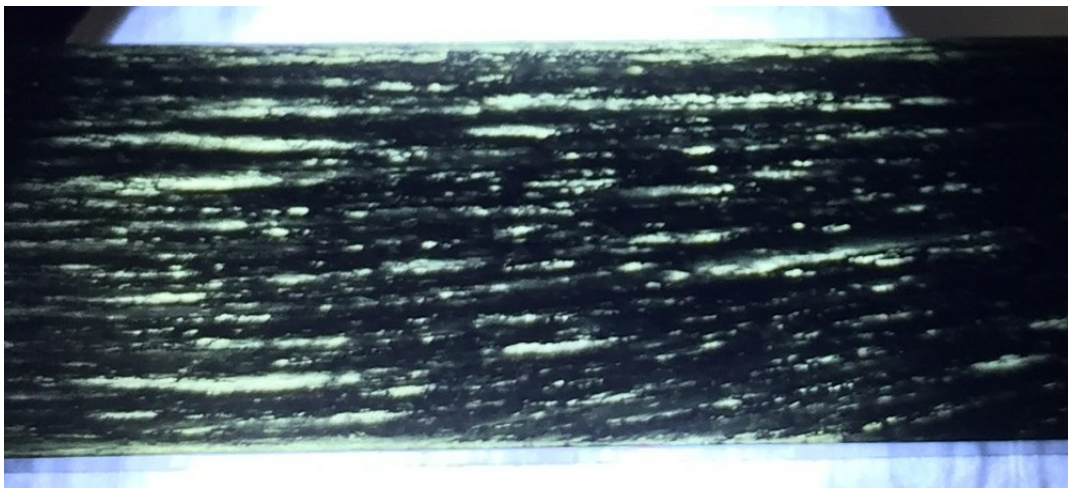

Figure 2-2: Aligned Particles in Terfenol-D/Epoxy Composite

Chapter 3

Fiber Bragg Grating

3.1 Introduction

Typically, a Bragg grating is a periodic structure with a set of N uniformly spaced identical multilayer segments. In common analysis, secondary reflections are ignored as they contribute minuscule change. The wave transfer matrix (M-matrix) may be the simplest way to understand the concept of the fiber Bragg grating [22]. It relates the waves at location 1 (backward wave amplitude $U_1^{(-)}$ and forward wave amplitude $U_1^{(+)}$)to those at location 2 (backward wave amplitude $U_2^{(-)}$ and forward wave amplitude $U_2^{(+)}$)

$$\begin{bmatrix} U_2^{(+)} \\ U_2^{(-)} \end{bmatrix} = \begin{bmatrix} A & B \\ C & D \end{bmatrix} \begin{bmatrix} U_1^{(+)} \\ U_1^{(-)} \end{bmatrix}, \tag{3.1}$$

with A, B, C, and D being the characteristics of an optical device. One may also consider a wave scattering matrix (S-matrix) for better connection to the physical process of reflection and transmission of the input waves. S-matrix is based off of amplitude transmittances (t_{12} and t_{21}) and reflectances (r_{12} and r_{21})

$$\begin{bmatrix} U_2^{(+)} \\ U_1^{(-)} \end{bmatrix} = \begin{bmatrix} t_{12} & r_{21} \\ r_{12} & t_{21} \end{bmatrix} \begin{bmatrix} U_1^{(+)} \\ U_2^{(-)} \end{bmatrix}. \tag{3.2}$$

r_{12} and t_{12} are for a wave traveling from medium one to medium two, and vice versa for r_{21} and t_{21}. The M-matrix is more straight forward for cascading, such that if n-segments are considered, $M_{tot} = M_n M_{n-1} \cdots M_1 M_0$. Figure 3-1 shows the difference between the M-matrix (**M**) and the S-matrix (**S**).

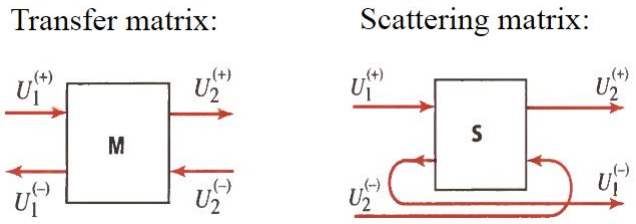

Figure 3-1: Transfer Matrix and Scattering Matrix

Their conversion relationships are as follows

$$M = \frac{1}{t_{21}} \begin{bmatrix} t_{12}t_{21} - r_{12}r_{21} & r_{21} \\ -r_{12} & 1 \end{bmatrix} \tag{3.3}$$

and

$$S = \frac{1}{D} \begin{bmatrix} AD - BC & B \\ -C & 1 \end{bmatrix}. \tag{3.4}$$

Several scenarios are possible for the transfer matrix. The first to consider is propagation through a homogeneous medium. In this case,

$$U_2^{(+)} = AU_1^{(+)} + BU_1^{(-)}, \tag{3.5}$$

$$U_2^{(-)} = CU_1^{(+)} + DU_1^{(-)}. \tag{3.6}$$

For which no reflection should take place such that B=C=0. $U_2^{(+)}$ and $U_2^{(-)}$ incur phase shifts $-kd$ and kd respectively so that $A = e^{-jkd}$ and $D = e^{jkd}$. From this, the transfer

matrix can be written as

$$\begin{bmatrix} U_2^{(+)} \\ U_2^{(-)} \end{bmatrix} = \begin{bmatrix} e^{-jkd} & 0 \\ 0 & e^{jkd} \end{bmatrix} \begin{bmatrix} U_1^{(+)} \\ U_1^{(-)} \end{bmatrix}, \tag{3.7}$$

and the scattering matrix can be written as

$$\begin{bmatrix} U_2^{(+)} \\ U_1^{(-)} \end{bmatrix} = \begin{bmatrix} e^{-jkd} & 0 \\ 0 & e^{-jkd} \end{bmatrix} \begin{bmatrix} U_1^{(+)} \\ U_2^{(-)} \end{bmatrix}. \tag{3.8}$$

The next application to consider is a dielectric boundary with different refractive indices. From the Fresnel Equations, the transmission from medium one to medium two is given by $t_{12} = \frac{2n_1}{n_1+n_2}$ and the reflection is given by $r_{12} = \frac{n_1-n_2}{n_1+n_2}$. Then the S-matrix can be represented as

$$\begin{bmatrix} U_2^{(+)} \\ U_1^{(-)} \end{bmatrix} = \frac{1}{n_1+n_2} \begin{bmatrix} 2n_1 & n_2-n_1 \\ n_1-n_2 & 2n_2 \end{bmatrix} \begin{bmatrix} U_1^{(+)} \\ U_2^{(-)} \end{bmatrix}, \tag{3.9}$$

and be converted into the following M-matrix

$$\begin{bmatrix} U_2^{(+)} \\ U_2^{(-)} \end{bmatrix} = \frac{1}{2n_2} \begin{bmatrix} n_2+n_1 & n_2-n_1 \\ n_2-n_1 & n_2+n_1 \end{bmatrix} \begin{bmatrix} U_1^{(+)} \\ U_1^{(-)} \end{bmatrix}. \tag{3.10}$$

If the previous two M-matrices are combined as shown in Figure 3-2, then the complete M-matrix is written as

$$\begin{bmatrix} U_2^{(+)} \\ U_2^{(-)} \end{bmatrix} = \frac{1}{2n_2} \begin{bmatrix} (n_2+n_1)e^{-jkd} & (n_2-n_1)e^{jkd} \\ (n_2-n_1)e^{-jkd} & (n_2+n_1)e^{jkd} \end{bmatrix} \begin{bmatrix} U_1^{(+)} \\ U_1^{(-)} \end{bmatrix}, \tag{3.11}$$

where e^{-jkd} can be written as $e^{-j\phi}$ with $\phi = kd = nk_0d$. For a lossless reciprocal medium, such as a partially reflective mirror, $|t_{12}| = |t_{21}| = |t|$, $|r_{12}| = |r_{21}| = |r|$, $|t^2| + |r^2| = 1$ and $\frac{t_{12}}{t_{21}^*} = -\frac{r_{12}}{r_{21}^*}$.

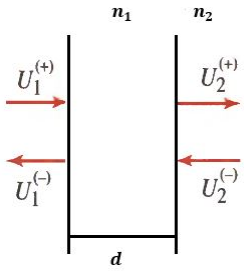

Figure 3-2: M-Matrix for a Propagation Distance of d and Dielectric Boundary between Media with Refractive Indices n_1 and n_2

Assuming $Arg(t) = 0$, the M-matrix and S- matrix are given as

$$M = \begin{bmatrix} \frac{1}{t^*} & \frac{r}{t} \\ \frac{r^*}{t^*} & \frac{1}{t} \end{bmatrix} = \frac{1}{|t|} \begin{bmatrix} 1 & j|r| \\ -j|r| & 1 \end{bmatrix}, \tag{3.12}$$

$$S = \begin{bmatrix} t & r \\ r & t \end{bmatrix} = \begin{bmatrix} |t| & j|r| \\ j|r| & |t| \end{bmatrix}. \tag{3.13}$$

Figure 3-3 shows a system of cascading identical M-matrices with individual matrix as $\mathbf{M}_0$. From [22] and [23], since $\mathbf{M}_0$ is unimodular, the final M-matrix, $\mathbf{M}_0^N$, for a grating with a stack of N identical periods can be expressed as

$$\mathbf{M}_0^N = \Psi_N \mathbf{M}_0 - \Psi_{N-1}\mathbf{I}, \tag{3.14}$$

where

$$\Psi_N = \frac{\sin(N\Phi)}{\sin\Phi}, \tag{3.15}$$

and

$$\cos(\Phi) = Re\left(\frac{1}{t}\right). \tag{3.16}$$

Ψ_N is the interference factor and $\mathbf{I}$ is the identity matrix. The final matrix is also unimodular and can be expressed as

$$\mathbf{M}_0^N = \begin{bmatrix} \frac{1}{t_N^*} & \frac{r_N}{t_N} \\ \frac{r_N^*}{t_N^*} & \frac{1}{t_N} \end{bmatrix}, \tag{3.17}$$

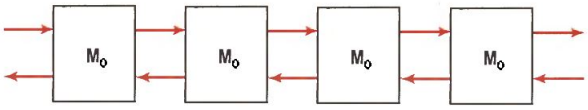

Figure 3-3: Cascading of Identical M-Matrices $\mathbf{M}_0$

where t_N and r_N are the N^{th}-segment amplitude transmittance and reflectance. Basing on Eqs. (3.14) and (3.17), a recursive relation can be formulated.

$$\frac{1}{t_N} = \Psi_N \frac{1}{t} - \Psi_{N-1}, \tag{3.18}$$

$$\frac{r_N}{t_N} = \Psi \frac{r}{t}. \tag{3.19}$$

The power transmittance is defined by $T_N = |t_N|^2$. Also the power reflectance is given by $R_N = 1 - T_N$. Applying them to Eqs. (3.18) and (3.19),

$$T_N = \frac{T}{T + \Psi_N^2(1-T)}, \tag{3.20}$$

$$R_N = \frac{\Psi_N^2 R}{1 - R + \Psi_N^2 R}. \tag{3.21}$$

3.2 Optical Properties

From the previous section, there are two different kinds of reflection regimes. They are the partial-reflection regime and the total-reflection regime. The interference factor Ψ_N is very dependent on $\Phi = \cos^{-1}(Re[1/t])$. Partial reflection occurs when $|Re[1/t]| \leq 1$. This allows for Φ to be real. For total reflection regime, $|Re[1/t]| > 1$ implies Φ to be complex and $\cos\Phi$ to be real, i.e. $\Phi = \Phi_R + j\Phi_I$ and $Im(\cos\Phi) = 0$. Since $\cos(\Phi_R + j\Phi_I) = \cos(\Phi_R)\cosh(\Phi_I) - j\sin(\Phi_R)\sinh(\Phi_I)$, Φ_R must be equal to zero. This result causes a

significant change in the reflectivity to

$$\cosh(\Phi_I) = \left| Re\left(\frac{1}{t}\right)\right|, \tag{3.22}$$

$$\Psi_N = \pm\frac{\sinh(N\Phi_I)}{\sinh(\Phi_I)}. \tag{3.23}$$

This allows for the reflection to be much larger due to the hyperbolic sine function. The following example presents the analysis of a scenario with partially reflective mirrors. Consider the M-matrix $\mathbf{M}_0$ as

$$M_0 = \frac{1}{|t|}\begin{bmatrix} e^{-j\phi} & j|r|e^{j\phi} \\ -j|r|e^{-j\phi} & e^{j\phi} \end{bmatrix}. \tag{3.24}$$

where $\phi = nk_0\Lambda = \frac{\pi\nu}{\nu_B}$ and Λ is the spacing between mirrors and $\nu_B = c/2\Lambda$ is the Bragg frequency. In terms of the S-matrix, the amplitude transmission can be defined as $t = |t|e^{j\phi}$ and Φ can be determined with

$$\cos(\Phi) = \frac{1}{|t|}\cos(\phi) \qquad for \qquad |\cos(\phi)| \leq |t| \tag{3.25}$$

$$\cosh(\Phi) = \frac{1}{|t|}|\cos(\phi)| \qquad for \qquad |\cos(\phi)| > |t|. \tag{3.26}$$

Figure 3-4 shows the power reflectance of a grating with $N = 10$ partially reflective mirrors with $|t|^2 = 0.5$.

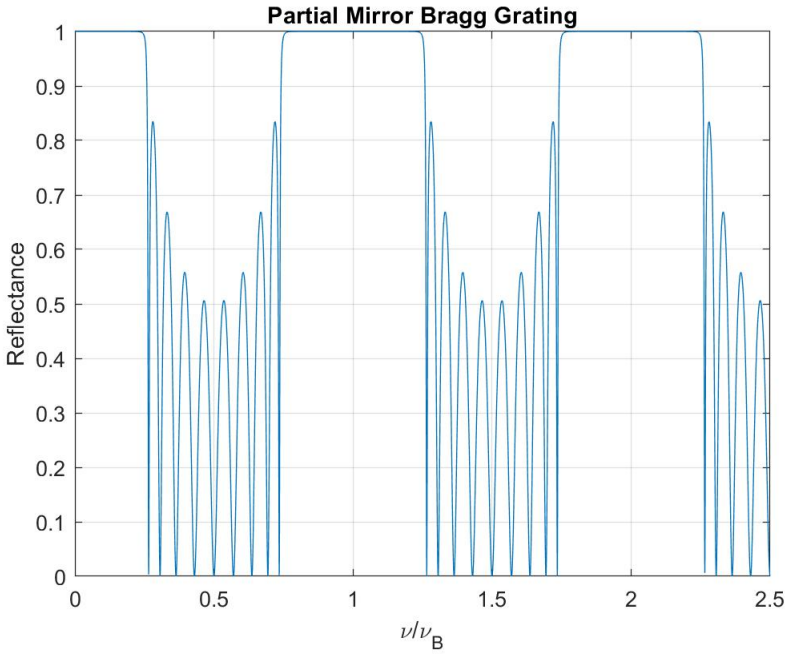

Figure 3-4: Reflectance From Cascaded Partial Reflective Mirrors

A dielectric Bragg grating is made of N identical periods in the refractive index modulation. By cascading two M-matrices in from of Eq. (3.11) to account for two propagation distances ($d = d_1$ and $d = d_2$) and two dielectric boundaries (from n_1 to n_2 and from n_2 to n_1), the M-matrix for the grating can be constructed such that

$$Re\left[\frac{1}{t}\right] = \frac{(n_1+n_2)^2}{4n_1n_2}\cos(\phi_1+\phi_2) - \frac{(n_2-n_1)^2}{4n_1n_2}\cos(\phi_1-\phi_2), \tag{3.27}$$

with $\phi_1 = k_0 n_1 d_1$ and $\phi_2 = k_0 n_2 d_2$ corresponding to the phases introduced by the two layers of the different dielectrics. From this, the spectral dependence is determined by $\phi_1 + \phi_2 = \pi\nu/\nu_B$. Figure 3-5 shows the power reflectance for a dielectric Bragg grating with $N = 10$ for indices of $n_1 = 1.5$ and $n_2 = 3.5$.

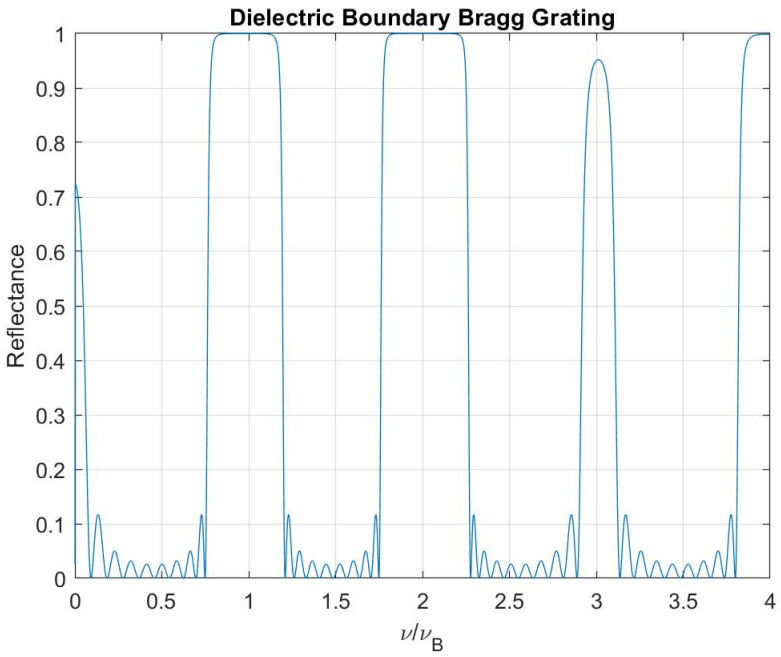

Figure 3-5: Reflectance From Cascaded Dielectric Boundaries

This chapter serves as the brief introduction to the concept of a Bragg grating in an optical system. That being said, a more complex analysis is needed to produce a precise outcome as the M-matrix in here has built-in assumptions within the model compared to an electromagnetic analysis of FBG. Chapter 4 will show a more general approach for analyzing an FBG that is capable of modeling index modulations in various forms by treating them as perturbations.

Chapter 4

Theoretical Analysis

4.1 Magnetization Due to Geometry

The purpose of this section is to analyze the magnetic field intensity inside of a magnetic body. Owing to the geometry of a magnetic body, the magnetic field intensity inside the magnetic body can vary along the direction of an external field even through the external field is uniform. The distribution of the internal magnetic field intensity causes a non-uniform magnetostrictive response that is coupled to an FBG. Two geometries are considered here - a trapezoidal slab and an approximation of an acute Saccharin quadrilateral slab.

4.1.1 Magnetic Field Inside a Magnetic Body

This section uses unprimed and primed coordinates where $\vec{r}$ is the position vector from the origin to the observation point and $\vec{r}'$ is the position vector from the origin to source point inside the magnetic body. Consider Maxwell's equations for static fields with

$$\nabla \times \vec{B} = 0. \tag{4.1}$$

This means that the magnetic flux density is curl-free and can be expressed as either the divergence of a vector or as the gradient of a scalar field. The scalar magnetic potential

V_m [24] will be investigated such that

$$\vec{H}_{dmg} = -\nabla V_m. \tag{4.2}$$

where $\vec{H}_{dmg}$ is the equivalent magnetic field intensity caused by the magnetization vector $\vec{M}$ of the magnetic body and the negative sign follows the opposite convention between field and potential. The scalar magnetic potential is expressed as,

$$V_m = \int_{V'} \frac{\vec{M} \cdot \hat{R}}{4\pi R^2} dv' \tag{4.3}$$

where $\hat{R} = \frac{\vec{R}}{R}$ and $\vec{R} = \vec{r} - \vec{r}'$. Now it is key to note that a substitution can be made because

$$\frac{\hat{R}}{R^2} = \nabla' \frac{1}{R}. \tag{4.4}$$

This allows for Eq. (4.3) to be expressed as

$$V_m = \frac{1}{4\pi} \int_{V'} \vec{M} \cdot \nabla' \frac{1}{R} dv' \tag{4.5}$$

with the vector identity

$$\begin{aligned} \nabla' \cdot (f\vec{A}) &= f\nabla' \cdot \vec{A} + \vec{A} \cdot \nabla' f \\ \vec{A} \cdot \nabla' f &= \nabla' \cdot (f\vec{A}) - f\nabla' \cdot \vec{A}, \end{aligned} \tag{4.6}$$

with $f = \frac{1}{R}$ and $\vec{A} = \vec{M}$. Substituting Eq. (4.6) into Eq. (4.5),

$$V_m = \frac{1}{4\pi} \int_{V'} \nabla' \cdot \left(\frac{\vec{M}}{R} \right) dv' - \frac{1}{4\pi} \int_{V'} \frac{\nabla' \cdot \vec{M}}{R} dv' \tag{4.7}$$

and if $\vec{M} = M_0 \hat{z}$ is uniform, i.e. constant M_0, then the second term will be equal to zero. For this research, the magnetization vector was assumed to be in the same direction of the uniform external field $H_{ext}\hat{z}$ along z. This assumption allows the derivation of analytical expression that can accurately approximate Eq. (4.7), especially for magnetic bodies with their longest dimension along z that is significantly larger than their widths. Furthermore,

the divergence theorem enables the approximation of Eq. (4.7) to be rewritten as

$$V_m \approx \frac{1}{4\pi} \oint_{S'} \frac{\vec{M} \cdot \hat{n}'}{R} dS' \tag{4.8}$$

where $\hat{n}'$ is the outward pointing normal of the magnetic body surface. Recall that $\vec{H}_{dmg} = -\nabla V_m$. As this vector field is the reaction to the external field, it usually opposes the external field. Hence, H_{dmg} is called the demagnetization field.

The FBG will be placed along the z-axis which is the long axis of the magnetic body and aligns with directions of $\vec{M}$ and $H_{ext}\hat{z}$. Therefore, a scalar equation can be obtained for the internal magnetic field intensity $H_{int}(z)$ along the z-axis

$$H_{int}(z) = H_{ext} + H_{dmg}(z). \tag{4.9}$$

$H_{dmg}(z)$ is the axial demagnetization field and is evaluated with the gradient of Eq. (4.8). M_0 is an unknown factor but is assumed to be approximately a product of magnetic property (the magnetic susceptibility, $\chi_m = 9$ for Terfenol-D) and $H_{int}(z)$, i.e. $M_0 \approx \chi_m H_{int}(z)$, for certain geometries where its length is much longer than the width. Thus, by this approximation, H_{ext} can be shown to be augmented by a demagnetization factor for determining $H_{int}(z)$.

Trapezoidal Slab

Consider a trapezoidal slab as shown in Figure 4-1, where the trapezoidal slab is very thin. This is desirable since an increase in slab thickness will further reduce the internal magnetic field intensity, but variations in thickness are required to modulate the internal magnetic field. For the sensor application, the internal field of the magnetic body is desired to be as close to the external field as possible to achieve higher sensitivity. Hence, the parallel sides are chosen to have minimum distance for maximum sensitivity but the slanted sides are designed to introduce field variation.

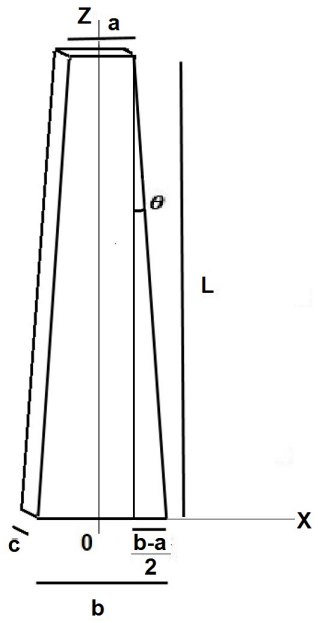

Figure 4-1: Trapezoidal Slab

The surface integral in Eq. (4.8) can be broken down into four integrals which consist of the top, bottom, and slanted surfaces. The remaining surfaces will be equal to zero since the magnetization vector is parallel to them. As $H_{dmg}(z)$ is mainly an axial field, $\vec{r} = z'\hat{z}$ and the distance between observation and source points $|\vec{R}|$ can be expressed explicitly in Cartesian coordinates as

$$R(z, z', y', x') = \sqrt{(z - z')^2 + x'^2 + y'^2}, \tag{4.10}$$

with the differential area $ds' = dx'dy'$. Thus the scalar potential for the top and bottom surfaces is

$$V_{mTB} = \frac{M_0}{\pi} \int_0^{c/2} \int_0^{a/2} \frac{dx'dy'}{R(z, L, y', x')} - \frac{M_0}{\pi} \int_0^{c/2} \int_0^{b/2} \frac{dx'dy'}{R(z, 0, y', x')}. \tag{4.11}$$

Owing to the rectangular symmetry of the top and bottom surfaces, only integrations over one quarter of the surfaces are required and the scalar potential becomes

$$V_{mTB} = \frac{M_0}{\pi} \int_0^{c/2} \left[G\left(z, L, y', \frac{a}{2}\right) - G\left(z, 0, y', \frac{b}{2}\right) \right] dy' \tag{4.12}$$

where the integrand $G(z,z',y',x') = \ln\left(\frac{x'+R(z,z',y',x')}{R(z,z',0,x')}\right)$. Recall that $\vec{H}_{dmg} = -\nabla V_m$, where the gradient is with respect to the unprimed coordinates. Hence, the order of the gradient and integral can be interchanged. Since the results from both orders of operations converge, this interchange is acceptable. Such process also results in a faster calculation. Taking gradient of the integrand yields

$$\nabla G(z,z',y',x') = \frac{z-z'}{R(z,z',y',x')[x'+R(z,z',y',x')]} - \frac{z-z'}{R(z,z',y',0)}. \tag{4.13}$$

Integrating Eq. (4.13) over y' provides results in terms of a general function $F(z,z',y',x')$ that describes the spatial variation of the demagnetization field $(H_{dmg}(z))_{TB}$ caused by the top and bottom surfaces

$$\int \nabla G(z,z',y',x')dy' = F(z,z',y',x') - F(z,z',y',0) + C \tag{4.14}$$

where $F(z,z',y',x') = 2\,sgn(z-z')\tan^{-1}\left(\sqrt{\frac{R(z,z',0,x')-x'}{R(z,z',0,x')+x'}}\sqrt{\frac{R(z,z',y',x')-R(z,z',0,x')}{R(z,z',y',x')+R(z,z',0,x')}}\right)$ and C is the integration constant that can be eliminated after the substitution of limits of integration. Since special cases of $x'=0$ and $y'=0$, the general functions can be readily simplified into $F(z,z',y',0) = \tan^{-1}\left(\frac{y'}{z-z'}\right) + C$ and $F(z,z',0,x') = C$ respectively, $(H_{dmg}(z))_{TB}$ can be written into an expression with four terms:

$$(H_{dmg}(z))_{TB} = -\frac{M_0}{\pi}\left[F\left(z,L,\frac{c}{2},\frac{a}{2}\right) - \tan^{-1}\left(\frac{c}{2(z-L)}\right) - F\left(z,0,\frac{c}{2},\frac{b}{2}\right) + \tan^{-1}\left(\frac{c}{2z}\right)\right]. \tag{4.15}$$

For the complete determination of $H_{dmg}(z)$, the demagnetization $(H_{dmg}(z))_{Sides}$ from the side components must be considered, i.e.

$$H_{dmg}(z) = (H_{dmg}(z))_{TB} + (H_{dmg}(z))_{Sides}. \tag{4.16}$$

In the following subsection, the calculation of $(H_{dmg}(z))_{Sides}$ is discussed.

Slanted Components

For one slanted component, an angle θ will be defined as

$$\tan\theta = \frac{b-a}{2L'}, \tag{4.17}$$

with $L' = L$, full length of the slab. This angle will be of use for both the dot product of the numerator and for the denominator of the integrand for the scalar potential calculation. The differential surface area will consist of $dS' = dl'dy'$ where dl' is the hypotenuse of the right triangle from the figure above which can also be expressed as $\frac{dx'}{\sin\theta}$. The scalar potential for the slanted sides can be expressed similar to those for the base and the top as

$$V_{mSides} = \frac{M_0}{\pi}\int_0^{c/2}\int_{a/2}^{b/2}\frac{dx'dy'}{R(z,z'(x'),y',x')}. \tag{4.18}$$

Because of the normal vector to the surface, $\vec{M}\cdot\hat{n}' = M_0\sin\theta$ and this integral was multiplied by four due to the symmetry over the x'-axis and accounting for the other side of the trapezoidal slab. One issue that pertains this integral is the z' as a function of x' as denoted in the denominator of the integrand in Eq. (4.18). With $z' = 0$, $x' = \frac{b}{2}$. At $z' = L'$, $x' = \frac{a}{2}$, an equation of the line for the slanted side on positive x half plane can be constructed

$$z' = mx' + z_0 \tag{4.19}$$

where $m = -\cot\theta$ is the slope and $z_0 = \frac{b\cot\theta}{2}$ is the z' intercept. Substituting this to replace z' in Eq. (4.18)

$$V_{mSides} = \frac{M_0}{\pi\sqrt{1+m^2}}\int_0^{L}\int_{a/c}^{b/2}\frac{dx'dy'}{\tilde{R}(z,y',x')} \tag{4.20}$$

where $\tilde{R}(z,y',x') = \sqrt{D^2(z,y') + X^2(z,x')}$, $D(z,y') = \sqrt{(1-m^2)Z^2(z) + Y^2(y')}$, $Z(z) = \frac{z-z_o}{1+m^2}$, $Y(y') = \frac{y'}{\sqrt{1+m^2}}$, $X(z,x') = x' - x_s(z)$ and $x_s(z) = mZ(z)$. After integrating over x',

$$V_{mSides} = \frac{M_0}{\pi} \int_0^{c/2} \left[\tilde{G}\left(z, y', \frac{a}{2}\right) - \tilde{G}\left(z, y', \frac{b}{2}\right) \right] dy' \tag{4.21}$$

where $\tilde{G}(z,y',x') = \frac{1}{\sqrt{1+m^2}} \ln \left| \frac{X(z,x')}{D(z,y')} + \sqrt{1 + \left(\frac{X(z,x')}{D(z,y')}\right)^2} \right|$. The absolute value terms may be dropped since there is no chance of being negative. Similar to calculations for the top and bottom surfaces, Taking gradient of the integrand yields

$$\nabla\tilde{G}(z,y',x') = -\frac{1}{m(1+m^2)\tilde{R}(z,y',x')} \left(m^2 + \frac{x_s(z)X(z,x')}{D^2(z,y')} \right). \tag{4.22}$$

Integrating Eq. (4.22) over y' provides results in terms of a rather complicated function $\tilde{F}(z,x')$ that describes the spatial variation of the demagnetization field $(H_{dmg}(z))_{Sides}$ caused by the side surfaces

$$\int_0^{c/2} \nabla\tilde{G}(z,y',x')dy' = \tilde{F}(z,x') \tag{4.23}$$

where $\tilde{F}(z,x') = -\frac{1}{1+m^2} \left[m \ln \left| \frac{c}{2D(x',z)} + \sqrt{1 + \left(\frac{c}{2D(x',z)}\right)^2} \right| + \tan^{-1} \left(\frac{x'-x_s(z)}{Z(z)} \frac{c}{2\sqrt{D^2(x',z) + \left(\frac{c}{2}\right)^2}} \right) \right]$. Finally, $(H_{dmg}(z))_{Sides}$ can be written into an expression with two terms:

$$(H_{dmg}(z))_{Sides} = \frac{M_0}{\pi} \left[\tilde{F}\left(z, \frac{b}{2}\right) - \tilde{F}\left(z, \frac{a}{2}\right) \right]. \tag{4.24}$$

Now $H_{dmg}(z)$ can be determined by substituting Eqs. (4.15) and (4.24) into Eq. (4.16) with the approximation $M_0 \approx \chi_m H_{int}(z)$ applied. The resulting expression is then substituted into Eq. (4.9) to obtain

$$H_{int}(z) = \frac{H_{ext}(z)}{1 - \chi_m \left(\frac{H_{dmg}(z)}{M_0} \right)}. \tag{4.25}$$

The above computations are performed with Matlab. Figure 4-2 shows the internal magnetic field based on these analytical calculations for dimensions used in the fabrication of the

first magnetostrictive trapezoid slab where $a = 5.29mm$, $b = 10.21mm$, $c = 3.18mm$, $L' = L = 40mm$, and $\chi_m = 9$.

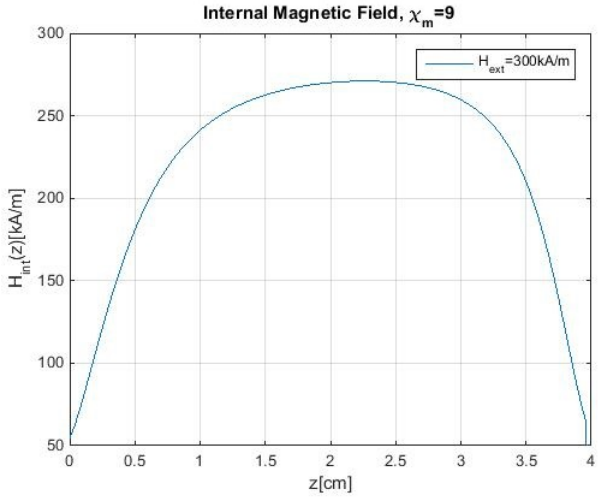

Figure 4-2: Internal Magnetic Field of Trapezoid Slab

Figure 4-3 shows the comparison between the analytical approximation and the numerical simulation with COMSOL. From Eq. (4.8), the approximation is made that the magnetization can be thought of as almost constant such that the volume integral in Eq. (4.7) can be neglected. This approximation is not assumed in COMSOL which provides the exact solution. Thus, the COMSOL results are more accurate and will be used for the internal field, which will then be related to the magnetization. For the COMSOL modeling, a trapezoidal slab was constructed the same slab dimensions as those used in analytical calculations.

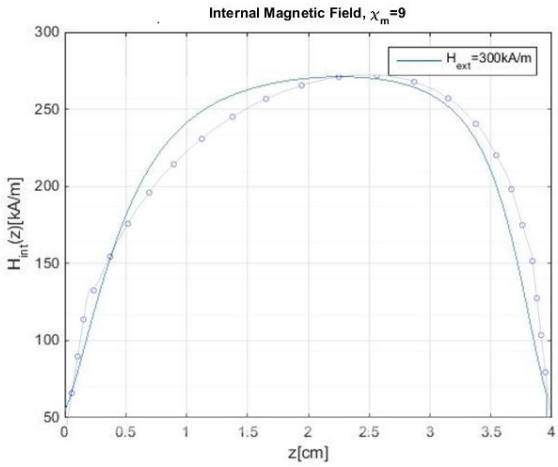

(a) Verification of Theoretical Approximation for Internal Magnetic Field with COMSOL

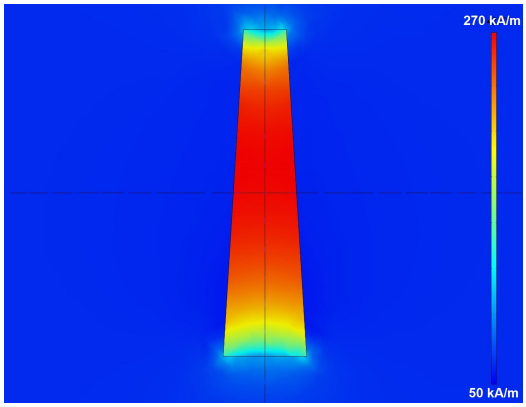

(b) COMSOL Simulation of Internal Field Distribution in a Trapezoidal Slab

Figure 4-3: COMSOL Comparison to Theoretical Predictions

For the trapezoidal slab, if the FBG is centered along the z-axis of the sample, a portion of it has a positive gradient in the strain that induces a positive chirp on the signal returned by the FBG while the remaining portion negative strain gradient that reduces the chirping. By changing the geometry of the sample, it is possible to achieve an extended region with a positive gradient which should enhance chirping constructively. An approximately acute Saccharin quadrilateral slab is shown to have potential in increasing the percentage length of the slab with positive strain gradient while the appropriate FBG placement along the z-axis further ensures its exposure to positive strain gradient only.

Approximation of an Acute Saccharin Quadrilateral Slab

Using a wider base can increase the positive gradient of the magnetization inside the sample, but also decreases the peak internal magnetic field. For this reasoning, an approximately acute Saccharin quadrilateral slab was investigated. Figure 4-4 shows the geometry of the slab under consideration. In fact, the geometry is equivalent to stack a rectangular bar at the narrow end of a trapezoid. Hence, the same computational method for the trapezoidal slab can be used for this new geometry, with the exception of the height of the trapezoid L' being less than L, i.e. the reduction in the length of the slanted components. This

modification leads to the increase in θ and the length of the narrow top that will reduce the demagnetization and push the internal magnetic field up. Figure 4-5 shows the internal magnetic field for different values for L'. The internal magnetic field for the potentially optimal geometry of the slab is shown in Figure 4-6 for a base width $b = 15mm$ and a top width $a = 5.29mm$. The length of the slanted components is shown to be $L' = 0.7L$.

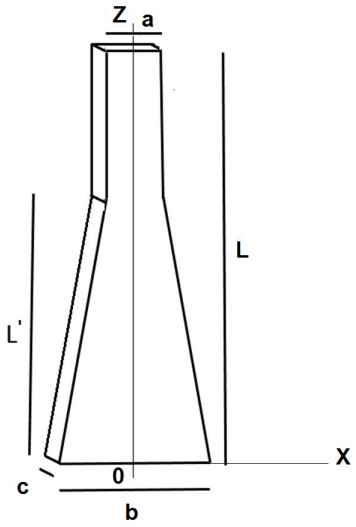

Figure 4-4: Approximately Acute Saccharin Quadrilateral Slab

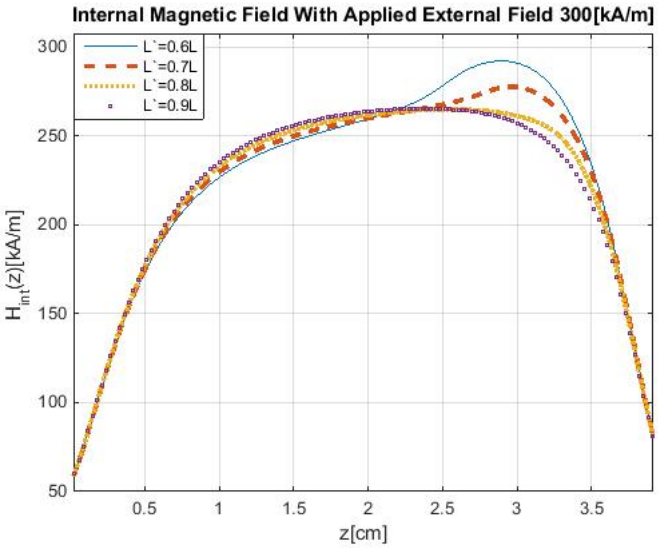

Figure 4-5: Internal Magnetic Field of Approximately Acute Saccharin Quadrilateral Slab with Different L's

The dimensions of the new sample were the same as the trapezoid slab, i.e. $a = 5.29mm$, $b = 10.21mm$, $c = 3.18mm$, and $L = 40mm$ except that $L' = 0.7L$. This was found to be optimal by locating the position with maximum internal magnetic field by taking the derivative of the internal magnetic field with respect to z, and identifying the point with a zero derivative beyond which the field gradient becomes negative. Ideally, the full FBG should be in between the wide base and this point to enhance chirping. Hence, the choice for L' is also limited by the FBG length of 3cm. As a result, $L' = 0.7L$ is the optimal value for achieving maximum chirping under this constraint.

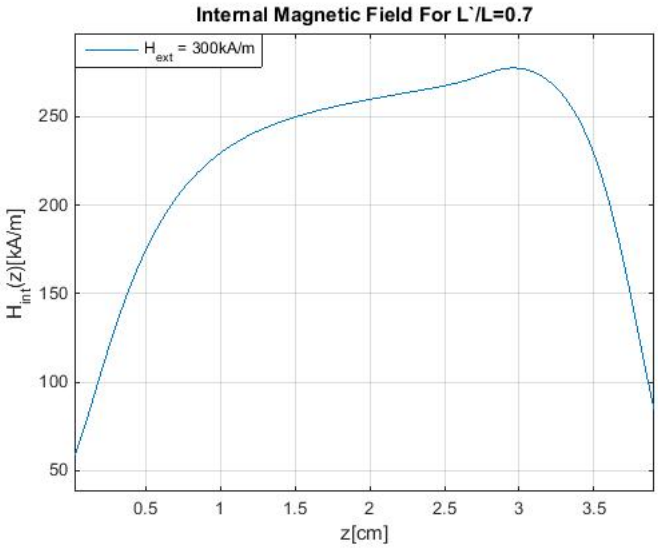

Figure 4-6: Internal Magnetic Field of Approximately Acute Saccharin Quadrilateral Slab with Optimal Dimensions

Figure 4-7 shows the comparison between the analytical calculation and the numerical simulation with COMSOL for the internal magnetic field. According to the internal magnetic field of the approximately acute Saccharin quadrilateral slab, placing the FBG at the base of the sample will ensure the maximum exposure to the positive field gradient. The goal of the geometric design is to have a more linear-like internal magnetic field with positive slope.

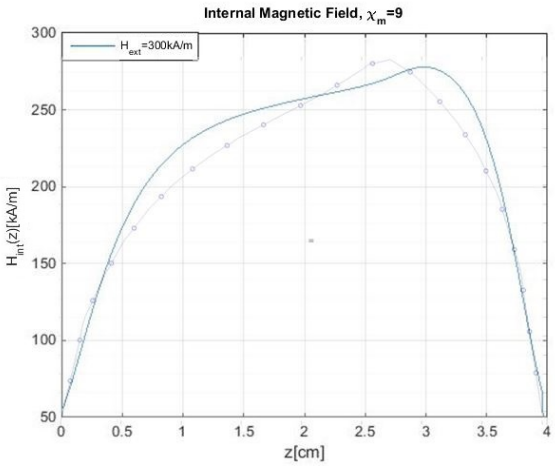

(a) Verification of Theoretical Calculation for Internal Magnetic Field with COMSOL

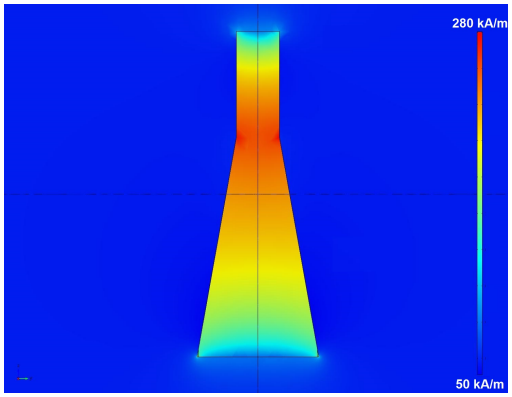

(b) COMSOL Simulation of Internal Field Distribution in an Approximately Acute Saccharin Quadrilateral Slab

Figure 4-7: COMSOL Comparison to Analytical Approximation

4.2 Optical Waveguide

For an optical waveguide with its axis along z-axis, propagating modes must satisfy the Maxwell's equations under boundary conditions of the waveguide.

$$\nabla \times \vec{E_\eta} = -j\omega\mu\vec{H_\eta}, \tag{4.26}$$

$$\nabla \times \vec{H_\eta} = j\omega\varepsilon\vec{E_\eta}. \tag{4.27}$$

$\vec{E_\eta}$ and $\vec{H_\eta}$ are the complex electric and magnetic field vectors respectively describing a general field distribution of x, y and z for a certain mode with positive index η of the waveguide with permeability μ and permittivity ε. For a dielectric waveguide, μ is assumed to be a constant while $\varepsilon = \varepsilon(x, y)$ under ideal condition. The Maxwell's equations are expressed in time harmonic form with time dependence $e^{j\omega t}$ where ω is the angular frequency of the field. It is natural to decompose fields and curl operator into transverse (t) and longitudinal (z) parts

$$\vec{E_\eta} = \vec{E}_{\eta t} + \vec{E}_{\eta z}, \tag{4.28}$$

$$\vec{H_\eta} = \vec{H}_{\eta t} + \vec{H}_{\eta z}, \tag{4.29}$$

$$(\nabla \times \vec{H}_\eta)_t = \nabla_t \times \vec{H}_{\eta z} + \hat{z} \times \frac{\partial \vec{H}_{\eta t}}{\partial z}, \tag{4.30}$$

$$(\nabla \times \vec{H}_\eta)_z = \nabla_t \times \vec{H}_{\eta t}, \tag{4.31}$$

where $\nabla = \nabla_t + \hat{z}\frac{\partial}{\partial z}$. Considering the longitudinal part of the curl operators in the Maxwell's equations, one can express the longitudinal part of an electric field in terms of the transverse part of the corresponding magnetic field and vice versa:

$$\vec{H}_{\eta z} = -\frac{1}{j\omega\mu}\nabla_t \times \vec{E}_{\eta t}, \tag{4.32}$$

$$\vec{E}_{\eta z} = \frac{1}{j\omega\varepsilon}\nabla_t \times \vec{H}_{\eta t}. \tag{4.33}$$

For the ideal optical waveguide with $\varepsilon = \varepsilon(x, y)$, fields for each mode are in the following forms:

$$\vec{H}_\eta = \pm\vec{h}_\eta(x, y)e^{\mp j\beta_\eta z}, \tag{4.34}$$

$$\vec{E}_\eta = \vec{e}_\eta(x, y)e^{\mp j\beta_\eta z}, \tag{4.35}$$

where β_η is the ηth modal propagation constant and modes with negative (positive) power propagate forward (backward). For backward propagating modes, the sign for $\vec{h}_{\nu t}(x, y)$ must be flipped owing to the convention of keeping $\vec{e}_{\nu t}(x, y)$ in the same polarity for both forward and backward propagating modes. With appropriate normalization for $\vec{e}_\eta(x, y)$ and $\vec{h}_\eta(x, y)$, the following orthogonality condition can be obtained

$$\int\int_S \vec{e}_{\nu t}(x,y) \times \vec{h}^*_{\eta t}(x,y) \cdot \hat{z} dS = \int\int_S \vec{e}^*_{\nu t}(x,y) \times \vec{h}_{\eta t}(x,y) \cdot \hat{z} dS = \pm 2 P_{avg} \delta_{\nu\eta} \tag{4.36}$$

where S represents an integration area over a large cross section, P_{avg} is time average power over S, the negative sign is for backward propagating modes and $\delta_{\nu\eta}$ is the Kronecker's delta function for discrete indices ν and η. For propagating modes in an optical waveguide, $P_{avg} = \frac{1}{2\eta_w} \int\int_S \vec{e}^*_{\nu t}(x,y) \cdot \vec{e}_{\nu t}(x,y) dS$ where $\eta_w = \sqrt{\frac{\mu}{\varepsilon}}$ is the wave impedance.

4.2.1 Polarization Vector as a Source of Coupling

Owing to orthogonality of modes, there is no coupling among modes. Now the ideal optical waveguide is perturbed and becomes $\varepsilon = \varepsilon(x,y,z)$. As a result, fields $\vec{E}$ and $\vec{H}$ for the perturbed system are source-driven and not equal to $\vec{E}_\eta$ and $\vec{H}_\eta$ [25]. The Maxwell's equations are updated with a polarization vector $\vec{P}$ that accounts for z dependence of ε

$$\nabla \times \vec{E} = -j\omega\mu\vec{H}, \tag{4.37}$$

$$\nabla \times \vec{H} = j\omega\varepsilon\vec{E} + j\omega\vec{P}. \tag{4.38}$$

Applying the divergence of vector cross products between fields in the ideal system and the perturbed system, one can reveal the coupling among modes in the perturbed system

$$\nabla \cdot \vec{\mathscr{S}} = -j\omega\vec{E}^*_\eta \cdot \vec{P} \tag{4.39}$$

where $\vec{\mathscr{S}} = \vec{E} \times \vec{H}^*_\eta + \vec{E}^*_\eta \times \vec{H}$. The vector identity

$$\nabla \cdot \vec{A} \times \vec{B} = \vec{B} \cdot \nabla \times \vec{A} - \vec{A} \cdot \nabla \times \vec{B} \tag{4.40}$$

and the Maxwell's equations are used to evaluate

$$\nabla \cdot (\vec{E} \times \vec{H}^*_\eta) = j\omega(\varepsilon\vec{E} \cdot \vec{E}^*_\eta - \mu\vec{H} \cdot \vec{H}^*_\eta), \tag{4.41}$$

and

$$\nabla \cdot (\vec{E}_\eta^* \times \vec{H}) = -j\omega(\vec{E}_\eta^* \cdot \vec{P} + \varepsilon \vec{E} \cdot \vec{E}_\eta^* - \mu \vec{H} \cdot \vec{H}_\eta^*). \tag{4.42}$$

Then the divergence theorem for a volume of infinitesimal thickness, similar to a pizza box, is applied to convert the differential form into an integral [26]

$$\int\int_S \nabla \cdot \vec{\mathscr{F}} = \frac{\partial}{\partial z} \int\int_S \vec{\mathscr{F}} \cdot \hat{z} dS + \oint_{l_S} \vec{\mathscr{F}} \cdot \hat{n} dl \tag{4.43}$$

where l_S is the perimeter of the large cross section and $\hat{n}$ is the outward pointing normal to the perimeter. For waveguide modes, field distributions have compact support and vanish at the perimeter, i.e. the length integral to be zero. Thus, (4.42) can be expressed as

$$\frac{\partial}{\partial z} \int\int_S \vec{\mathscr{F}} \cdot \hat{z} dS = -j\omega \int\int_S \vec{E}_\eta^* \cdot \vec{P} dS. \tag{4.44}$$

A modal expansion can be assumed of the modes in the waveguide such that

$$\vec{E}(x,y,z) = \vec{E}_{\eta t}(x,y,z) + \vec{E}_{\eta z}(x,y,z) = \sum_\nu (a_\nu(z) + b_\nu(z))(\vec{e}_{\nu t}(x,y) + (\vec{e}_{\nu z}(x,y)), \tag{4.45}$$

$$\vec{H}(x,y,z) = \vec{H}_{\eta t}(x,y,z) + \vec{H}_{\eta z}(x,y,z) = \sum_\nu (a_\nu(z) - b_\nu(z))(\vec{h}_{\nu t}(x,y) + \vec{h}_{\nu z}(x,y)). \tag{4.46}$$

There is a z-dependence on the modal coefficients. This is caused by the interaction among modes along the longitudinal direction due to a polarization source. The expansion coefficients can be expressed as $a_\nu(z) = A_\nu(z)e^{-j\beta_\nu z}$ for forward propagating modes and $b_\nu(z) = B_\nu(z)e^{j\beta_\nu z}$ for backward propagating modes where $A_\nu(z)$ and $B_\nu(z)$ are slowly varying envelopes of corresponding modal coefficients. For forward propagating modes such that $\vec{E}_\eta = \vec{e}_\eta(x,y)e^{-j\beta_\eta z}$ and $\vec{H}_\eta = \vec{h}_\eta(x,y)e^{-j\beta_\eta z}$ applying the orthogonality condition, Eq. (4.44) becomes

$$\frac{d}{dz}a_\eta(z)e^{j\beta_\eta z} = \frac{d}{dz}A_\eta(z) = -j\frac{\omega}{4}\int\int_S \left(\vec{e}^*_{\eta t}(x,y)e^{j\beta_\eta z} + \vec{e}^*_{\eta z}(x,y)e^{j\beta_\eta z}\right)\cdot\vec{P}dS. \quad (4.47)$$

Using similar procedure for backward modes with $\vec{E}_\eta = \vec{e}_\eta(x,y)e^{j\beta_\eta z}$ and $\vec{H}_\eta = -\vec{h}_\eta(x,y)e^{j\beta_\eta z}$, Eq. (4.44) yields the differential equation for the coefficient of the backward propagating modes

$$\frac{d}{dz}b_\eta(z)e^{-j\beta_\eta z} = \frac{d}{dz}B_\eta(z) == j\frac{\omega}{4}\int\int_S \left(\vec{e}^*_{\eta t}(x,y)e^{j\beta_\eta z} - \vec{e}^*_{\eta z}(x,y)e^{j\beta_\eta z}\right)\cdot\vec{P}dS. \quad (4.48)$$

The polarization vector can be written in terms of the electric field multiplied by the perturbation $\Delta\varepsilon$ which corresponds to the permittivity interaction [25], [27]. If the permittivity is anisotropic and causes a linear relation between the electric field and polarization, then the perturbation in permittivity $\Delta\varepsilon$ can be written as a tensor consisting of transverse $\Delta\varepsilon_t$ and longitudinal $\Delta\varepsilon_z$ components.

$$\Delta\varepsilon = \begin{bmatrix} \Delta\varepsilon_t & 0 \\ 0 & \Delta\varepsilon_z \end{bmatrix}. \quad (4.49)$$

This allows the polarization vector to be expressed as $\vec{P} = \Delta\varepsilon_t\vec{E}_t + \Delta\varepsilon_z\vec{E}_z$ which can also be expressed in the modal term for the transverse field

$$\vec{P} = \Delta\varepsilon_t\left(\sum_\nu (a_\nu(z) + b_\nu(z))\vec{e}_{\nu t}(x,y)\right) + \Delta\varepsilon_z\vec{E}_z. \quad (4.50)$$

Similar to Eq. (4.33), $\vec{E}_z$ can be expressed in terms of transverse part of the magnetic field vector

$$\vec{E}_z = \frac{1}{j\omega(\varepsilon + \Delta\varepsilon_z)}\nabla\times\vec{H}_t. \quad (4.51)$$

Expressing $\vec{H}_t$ in terms of the modal expansion,

$$\vec{E}_z = \frac{j\omega\varepsilon}{j\omega(\varepsilon + \Delta\varepsilon_z)} \left(\sum_{\nu} (a_\nu(z) - b_\nu(z)) \vec{e}_{\nu z}(x,y) \right). \tag{4.52}$$

The polarization vector can then be rewritten as

$$\vec{P} = \Delta\varepsilon_t \left(\sum_{\nu} (a_\nu(z) + b_\nu(z)) \vec{e}_{\nu t}(x,y) \right) + \frac{\varepsilon\Delta\varepsilon_z}{(\varepsilon + \Delta\varepsilon_z)} \left(\sum_{\nu} (a_\nu(z) - b_\nu(z)) \vec{e}_{\nu z}(x,y) \right). \tag{4.53}$$

Substituting Eq. (4.53) into Eqs. (4.47) and (4.48), coupled mode equations in terms of the envelopes $A_\nu(z)$ and $B_\nu(z)$ can be obtained

$$\frac{d}{dz}A_\eta(z) = -j \sum_{\nu} \left[A_\nu(z)(K^t_{\nu\eta} + K^z_{\nu\eta}) e^{-j(\beta_\nu - \beta_\eta)z} + B_\nu(z)(K^t_{\nu\eta} - K^z_{\nu\eta}) e^{j(\beta_\nu + \beta_\eta)z} \right], \tag{4.54}$$

$$\frac{d}{dz}B_\eta(z) = j \sum_{\nu} \left[A_\nu(z)(K^t_{\nu\eta} - K^z_{\nu\eta}) e^{-j(\beta_\nu + \beta_\eta)z} + B_\nu(z)(K^t_{\nu\eta} + K^z_{\nu\eta}) e^{j(\beta_\nu - \beta_\eta)z} \right]. \tag{4.55}$$

where the transverse coupling coefficient $K^t_{\nu\eta}$ and the longitudinal coupling coefficient $K^z_{\nu\eta}$ are defined as

$$K^t_{\nu\eta} = \frac{\omega}{4P_{avg}} \int\int_S \vec{e}^*_{\eta t}(x,y) \cdot \Delta\varepsilon_t \vec{e}_{\nu t}(x,y) dS, \tag{4.56}$$

$$K^z_{\nu\eta} = \frac{\omega}{4P_{avg}} \int\int_S \vec{e}^*_{\eta z}(x,y) \cdot \frac{\varepsilon\Delta\varepsilon_z}{(\varepsilon + \Delta\varepsilon_z)} \vec{e}_{\nu z}(x,y) dS. \tag{4.57}$$

For propagating modes, $|\vec{e}_{\nu t}(x,y)| >> |\vec{e}_{\nu z}(x,y)|$ in general. Hence, $K^z_{\nu\eta}$ can be neglected [25]. Owing to the fact that η and ν involve all possible modes, the system of coupled mode equations can be complicated. However, the analysis of FBG that is discussed next limits calculations to the coupling between two modes and complexity is reduced.

4.3 Modeling of FBG - Counterpropagating Coupled Waves

When considering the modeling of an FBG, the same coordinate system will be used as in the last section. An FBG is imprinted onto an optical fiber by exposing the fiber to a

ultra-violet light with periodic variations in intensity [28]. The fiber will be assumed to have no cross-sectional dependence on the position in the x-y-plane. The wave is propagating in the z-direction but the fields are oriented mostly in the transverse directions. The only dependence will be along the longitudinal (z-)direction where the field will see a periodic modulation in the permittivity. For FBGs, the perturbation in the permittivity can be expressed as in terms of $\delta\overline{n}_{eff}(z)$, the effective refractive index change spatially averaged over a grating period Λ

$$\Delta\varepsilon_t(z) \approx 2\varepsilon_0\overline{n}_{eff}(z)\delta\overline{n}_{eff}(z)\left[1+\upsilon\cos\left(\frac{2\pi}{\Lambda}z+\phi(z)\right)\right] \tag{4.58}$$

where ε_0 is the free space permittivity, υ is the fringe visibility that constitutes the modulation index and $\phi(z)$ is the phase introduced by the chirping in an FBG. Substituting Eq. (4.58) into Eq. (4.56), the z-dependence terms can be taken out of the integral since the differential area will not entail the z-direction

$$K^t_{\nu\eta} = \frac{\omega\varepsilon_0 n_{eff}}{2P}\delta\overline{n}_{eff}(z)\left[1+\upsilon\cos\left(\frac{2\pi}{\Lambda}z+\phi(z)\right)\right]\iint_S \vec{e}^{\,*}_{\eta t}(x,y)\cdot\vec{e}_{\nu t}(x,y)dS. \tag{4.59}$$

$K^t_{\nu\eta}$ can be rewritten in terms a "DC" coupling coefficient $\sigma_{\nu\eta}(z)$ and an "AC" coupling coefficient $\kappa_{\nu\eta}(z)$

$$K^t_{\nu\eta} = \sigma_{\nu\eta}(z) + 2\kappa_{\nu\eta}(z)\cos\left(\frac{2\pi}{\Lambda}z+\phi(z)\right) \tag{4.60}$$

where

$$\sigma_{\nu\eta}(z) = \frac{\omega\varepsilon_0 n_{eff}}{2P_{avg}}\delta\overline{n}_{eff}(z)\iint_S \vec{e}^{\,*}_{\eta t}(x,y)\cdot\vec{e}_{\nu t}(x,y)dS, \tag{4.61}$$

$$\kappa_{\nu\eta}(z) = \frac{\upsilon}{2}\sigma_{\nu\eta}(z). \tag{4.62}$$

The analysis of an FBG near resonance involves only the forward and backward modes with the same index, i.e. $\eta=\nu$, $A_\eta(z)=A_\nu(z)=A(z)$, $B_\eta(z)=B_\nu(z)=B(z)$ and the same propagation constant $\beta_\nu=\beta_\eta=\beta_0$. After dropping $K^z_{\nu\eta}$ and rewriting the cosine in Eq.

(4.60) as exponential functions , Eq. (4.54) can be reduced to

$$\begin{aligned}\frac{d}{dz}A(z) = -\,j\,\Big[A(z)\Big(\sigma(z)+\kappa(z)\Big[e^{j\left(\frac{2\pi}{\Lambda}z+\phi(z)\right)}+e^{-j\left(\frac{2\pi}{\Lambda}z+\phi(z)\right)}\Big]\Big)\\ +B(z)\Big(\sigma(z)e^{j2\beta_0 z}+\kappa(z)\Big[e^{j\left(2(\beta_0+\frac{\pi}{\Lambda})z+\phi(z)\right)}+e^{j\left(2(\beta_0-\frac{\pi}{\Lambda})z-\phi(z)\right)}\Big]\Big)\Big]\end{aligned} \tag{4.63}$$

where $\sigma(z) = \omega\varepsilon_0\eta_0\delta\overline{n}_{eff}(z) = \frac{2\pi}{\lambda_0}\delta\overline{n}_{eff}(z)$ with wave impedance in free space $\eta_0 = \sqrt{\frac{\mu_0}{\varepsilon_0}}$ and $\kappa(z) = \frac{v}{2}\sigma(z)$. Neglecting all fast oscillating terms, Eq. (4.63) becomes

$$\frac{d}{dz}A(z) = -j\sigma(z)A(z) - j\kappa(z)B(z)e^{j(\Delta\beta z-\phi(z))} \tag{4.64}$$

where $\Delta\beta = 2(\beta_0 - \frac{\pi}{\Lambda})$, $\beta_0 = \frac{2\pi n_{eff}}{\lambda_0}$, n_{eff} is the effective refractive index and λ_0 is the free space wavelength. Performing a similar procedure for $B(z)$, Eq. (4.55) becomes

$$\frac{d}{dz}B(z) = j\kappa(z)A(z)e^{-j(\Delta\beta z-\phi(z))} + j\sigma(z)B(z). \tag{4.65}$$

Formulating Eqs. (4.64) and (4.65) in terms of $R(z) = A(z)e^{-j\frac{\Delta\beta z-\phi(z)}{2}}$ and $S(z) = B(z)e^{j\frac{\Delta\beta z-\phi(z)}{2}}$,

$$\frac{d}{dz}R(z) = -j\delta(z)R(z) - j\kappa(z)S(z), \tag{4.66}$$

$$\frac{d}{dz}S(z) = j\kappa(z)R(z) + j\delta(z)S(z) \tag{4.67}$$

where $\delta(z) = \sigma(z) + \frac{1}{2}\left(\Delta\beta - \frac{d\phi(z)}{dz}\right)$.

Eqs. (4.66) and (4.67) constitute the modeling equation for FBGs, including chirped FBG and must be solved numerically. However, analytical solution does exist for a uniform FBG modeled by the differential equations with constant coefficients, i.e. $\phi(z) = \phi$, $\delta\overline{n}_{eff}(z) = \delta n_{eff}$, $\sigma(z) = \sigma = \frac{2\pi}{\lambda_0}\delta n_{eff}$, $\delta(z) = \delta = \sigma + \frac{\Delta\beta}{2}$ and $\kappa(z) = \kappa = \frac{v}{2}\sigma$. Eqs. (4.66) and (4.67) can be written in matrix form:

$$\frac{d}{dz}\mathbf{u} = \mathbf{M_c}\mathbf{u}, \tag{4.68}$$

where coupled mode matrix $\mathbf{M_c} = \begin{pmatrix} -j\delta & -j\kappa \\ j\kappa & j\delta \end{pmatrix}$ and column vector $\mathbf{u} = \begin{pmatrix} R(z) \\ S(z) \end{pmatrix}$. The eigenvalues λ of $\mathbf{M_c}$ are:

$$\lambda = \mp s \tag{4.69}$$

where $s = \sqrt{\kappa^2 - \delta^2}$. The corresponding eigenvectors are in form of $\mathbf{v} = \begin{pmatrix} 1 & \frac{\lambda + j\delta}{j\kappa} \end{pmatrix}^T$. Since $\mathbf{M_c}$ is unimodular, the matrix exponential $e^{\mathbf{M_c}z}$ constructed from similarity transform with λ and $\mathbf{v}$ must have the same property

$$e^{\mathbf{M_c}z} = \frac{j\kappa}{2s} \begin{pmatrix} 1 & 1 \\ \frac{-s+j\delta}{j\kappa} & \frac{s+j\delta}{j\kappa} \end{pmatrix} \begin{pmatrix} e^{-sz} & 0 \\ 0 & e^{sz} \end{pmatrix} \begin{pmatrix} \frac{s+j\delta}{j\kappa} & -1 \\ \frac{s-j\delta}{j\kappa} & 1 \end{pmatrix} \tag{4.70}$$

$$= \begin{pmatrix} \cosh sz - j\frac{\delta}{s}\sinh sz & -j\frac{\kappa}{s}\sinh sz \\ j\frac{\kappa}{s}\sinh sz & \cosh sz + j\frac{\delta}{s}\sinh sz \end{pmatrix}. \tag{4.71}$$

In the case of a uniform FBG, the "DC" coupling coefficient σ is not required since its effect has been accounted for during the modal calculations for the system with $\varepsilon = \varepsilon(x, y)$. Hence, $\delta = \frac{\Delta\beta}{2}$ and Eq. (4.71) becomes exactly the same as the corresponding FBG equation in Ref. 15. Now δ can be interpreted as the detuning from a resonance. At resonance, i.e. $\delta = 0$, λ_0 reaches the Bragg wavelength

$$\lambda_B = 2n_{eff}\Lambda \tag{4.72}$$

In fact, $e^{\mathbf{M_c}z}$ is the M-matrix $\mathbf{M_{FBG}}(\delta, s, z)$ relating modal envelopes at $z = 0$ (input end of an FBG) to those inside the FBG at z

$$\begin{bmatrix} R(z) \\ S(z) \end{bmatrix} = \mathbf{M_{FBG}}(\delta, s, z) \begin{bmatrix} R(0) \\ S(0) \end{bmatrix}. \tag{4.73}$$

For an FBG, $R(z)$ represents the transmitted portion and $S(z)$ represents the reflected portion. Figure 4-8 shows the initial conditions for an FBG length of $z = L$. The input into

the FBG ($R(0)$) can be normalized to unity, and at the end of the FBG, there is nothing entering from the opposite side, i.e. $S(L) = 0$. The two remaining unknown terms are $S(0)$ and $R(L)$, which represent the reflected light returning to the input side, and the transmitted light at the end of the FBG.

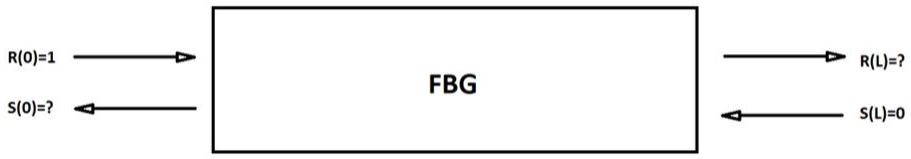

Figure 4-8: Initial Conditions for FBG

Eq. (4.72) can then be rewritten as,

$$\begin{bmatrix} R(L) \\ 0 \end{bmatrix} = \mathbf{M_{FBG}}(\delta, s, z) \begin{bmatrix} 1 \\ S(0) \end{bmatrix}. \tag{4.74}$$

The amplitude reflectance can be found by taking the ratio of reflected light at the input by the input light into the FBG. Since the input was normalized to unity, the amplitude reflectance ρ is just $S(0)$. In terms of the elements of $\mathbf{M_{FBG}}(\delta, s, L)$:

$$\rho = -\frac{[M(\delta, s, L)]_{21}}{[M(\delta, s, L)]_{22}} \tag{4.75}$$

where $[M(\delta, s, L)]_{21}$ and $[M(\delta, s, L)]_{22}$ are elements at (row 2, column 1) and (row 2, column 2) respectively. For an FBG length of 3cm, a refractive index of 1.45, a perturbation of the refractive index equal to 8×10^{-4}, and a fringe visibility of $\upsilon = 1$, Figure 4-9 shows the reflected spectrum.

For a non-uniform FBG, e.g. grating parameters depending on z, one can model it by breaking the FBG into multiple sections of FBGs with the sum of periods with all FBGs equal to the number of periods in the original FBG and the FBG at each section assuming the average parameters at that region [29], [30]. Now the M-matrix of the original FBG is

just the product of individual M-matrices for each section ordered in sequence following the variation of parameters:

$$\mathbf{M_{FBG}}(\delta, s, L) = \mathbf{M_{FBG_m}}(\delta_m, s_m, l_m) \dots \mathbf{M_{FBG_m}}(\delta_2, s_2, l_2)\mathbf{M_{FBG_m}}(\delta_1, s_1, l_1) \tag{4.76}$$

where δ_i, s_i, and l_i for $i = 1, \dots, m$ are parameters for individual FBGs and the length of the original FBG $L = \sum_{i=1}^{m} l_i$.

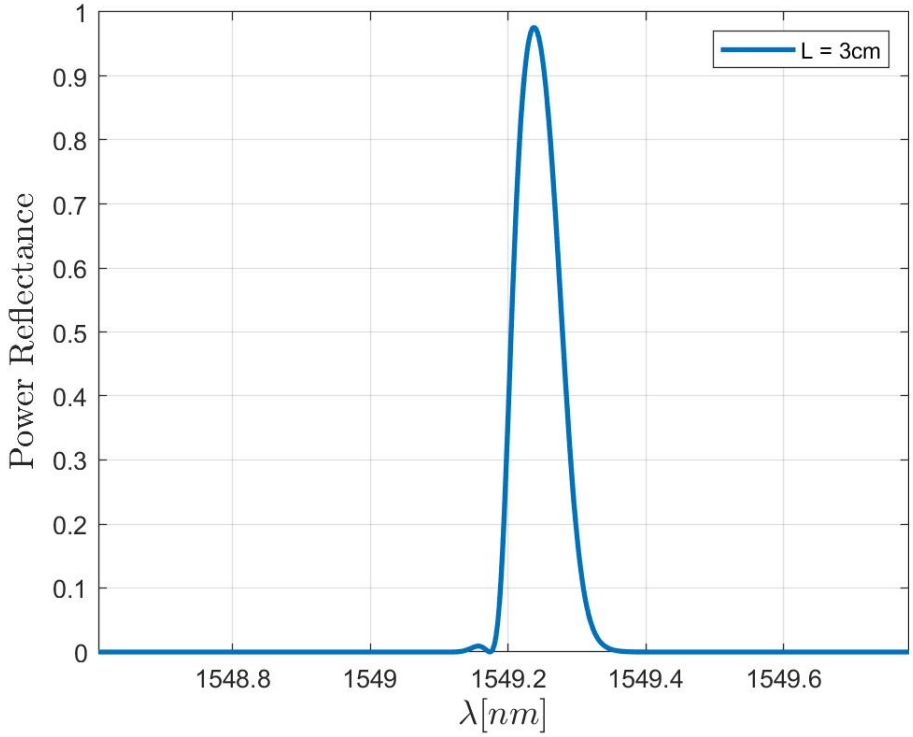

Figure 4-9: Power Reflectance of 3cm FBG Interaction

4.3.1 Theoretical Spectrum Shift Due to Strain

Uniform Strain Effect

If a uniform stress is placed along the FBG (z-)axis, each grating period will be strained the exactly same amount. As a result, the reflected spectrum is maintained the same shape but shifted to a different wavelength.

Non-Uniform Strain Effect

A non-uniform strain on the fiber will allow for things such as chirping to occur. As a thought-demonstration to understand the non-uniform grating, cascading of two gratings FBG_1 and FBG_2 with periods Λ_1 and Λ_2 ($\Lambda_1 \neq \Lambda_2$) respectively will be considered. If a polychromatic source is coupled to the fiber with the input end of FBG_1, all of the waves except a small frequency band will be transmitted through FBG_1 and continues to FBG_2. The reflected waves carry power P_1. From FBG_2, another small frequency band will be reflected back, but this reflected band has already been able to transmit through FBG_1. This results in the power P_2 from FBG_2 such that the total reflected power is a sum of the power from both gratings and is higher than the return from a single FBG. A key takeaway is that the reflected band from FBG_2 will transmit through FBG_1 since it would already have to travel through FBG_1 to get to FBG_2.

Recall that one way of describing the chirp factor is given by

$$\delta n_{eff}(z) = \overline{\delta} n_{eff} \left[1 + \upsilon \cos\left(\frac{2\pi}{\Lambda} z + \phi(z)\right)\right]. \tag{4.77}$$

The frequency chirping of the grating is controlled by $\phi(z)$ such that if the grating is uniform without chirping, $\frac{d\phi(z)}{dz} = 0$. Consider the alternating part of the perturbation of the refractive index as $\delta_{ac}(z) = \cos(k_g(z)z)$ where again in a uniform grating with constant period Λ, the wave number of the grating $k_g(z) = \frac{2\pi}{\Lambda}$. If a linear chirping effect is assumed, the grating length will gradually get longer as traveling along the z-axis. The grating period must be a function of z

$$\Lambda(z) = \Lambda_0 + \alpha_p z \tag{4.78}$$

where Λ_0 is the period at one end of the FBG and α_p is a fitting constant to define the linear strain. The new $k_g(z)$ term becomes

$$k_g(z) = \frac{2\pi}{\Lambda_0 + \alpha_p z}, \tag{4.79}$$

and by use of a Taylor series expansion for a small α_p can be written as

$$k_g(z) = \frac{2\pi}{\Lambda_0} - \frac{2\pi}{\Lambda_0^2}\alpha_p z. \tag{4.80}$$

Substituting this into the alternating term,

$$\delta_{ac}(z) = \cos\left(\frac{2\pi}{\Lambda_0}z - \frac{2\pi}{\Lambda_0^2}\alpha_p z^2\right). \tag{4.81}$$

This term can be related to $\cos\left(\frac{2\pi}{\Lambda}z + \phi(z)\right)$ where $\phi(z)$ now equals $-\frac{2\pi}{\Lambda_0^2}\alpha_p z^2$ and recall that $\delta(z) = \sigma(z) + \frac{1}{2}\left(\Delta\beta - \frac{d\phi(z)}{dz}\right)$ and $\omega = v_g\beta_0$ with v_g being the group velocity. The linear chirping of the FBG in ω becomes

$$\omega = \frac{v_g}{2}\frac{d\phi}{dz} = -\frac{2\pi v_g}{\Lambda_0^2}\alpha_p z. \tag{4.82}$$

The total chirping of the FBG will be dictated by the α_p value. Figure 4-10 shows the differences in reflection spectra based on different linear chirps for a 3cm FBG modeled in Figure 4-9 with a refractive index of 1.45, a perturbation of 8×10^{-4}, and a fringe visibility of $\upsilon = 1$. There is a clear distinction between stronger chirps and weak chirps. The spectrum broadens and the peak wavelength is shifted. This is expected as when there are uniform gratings, each grating will reflect the same wavelength. For the portion of the reflection wavelength that is not reflected from the first grating, the following gratings will be able to reflect. If there is a linear change in grating periods, the following gratings will not reflect the same wavelength, but will reflect a new wavelength which ensures spectral broadening. Determined by the average grating period, a new peak wavelength will be established for the common reflection wavelength of the FBG.

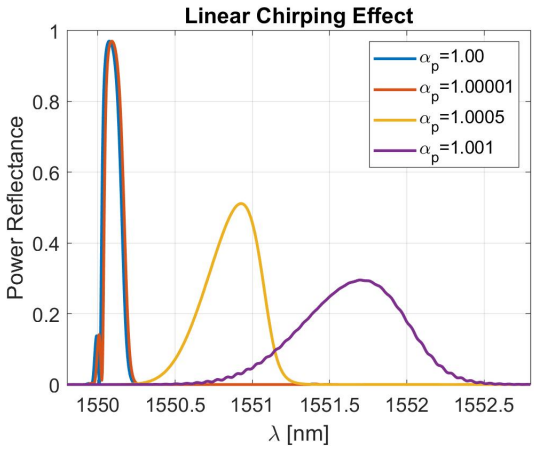

Figure 4-10: Spectra of a 3cm FBG with Linear Chirping Effect

4.3.2 Optical Properties From Strain Coupling to FBG

From the COMSOL simulations, a non-uniform magnetization is produced along the z-axis of the trapezoidal slab and the approximately acute Saccharin quadrilateral slab as discussed in Section 4.1. Different distributions of magnetization for each sample create different strain profiles that can be coupled to the embedded FBG through the modulation of Λ (see Section 4.2). Thus, the optical properties are able to be modified by the geometry of the magnetostrictive slab enabling the control of the sensor sensitivity.

Spectral Shift

The strain coupling to the fiber will produce a change in the gratings that can be expressed as

$$\Lambda(z) = \Lambda_0 + \Delta\Lambda(z), \tag{4.83}$$

and by taking an average over all the values, a peak wavelength can be calculated. This effect can be directly correlated to the magnetization controlled by the external magnetic field. From the previous equation,

$$\Delta\Lambda(z) = \Lambda_0(1 - P_{eff})\epsilon(M) + \Lambda_0((1 - P_{eff})(\alpha_m - \alpha_n) + \alpha_n + \zeta)\Delta T, \tag{4.84}$$

where

$$P_{eff} = \frac{n_{eff}^2}{2}(P_{12} - \nu(P_{11} + P_{12})). \tag{4.85}$$

n_{eff} is the effective refractive index of the fiber, ν refers to the Poisson ratio. P_{11} and P_{12} are the photo-elastic constants of silica [31]. P_{eff} is the total strain-optic effect which only entails the axial strain [32], [33]. ΔT, ζ, α_n, and α_m refer to thermal expansion effects which are not considered for this experiment since measurements took place in a temperature controlled room and sensing based on spectral width is immune from thermal effect [15]. The strain $\epsilon(M)$ is modeled with Eq. (2.36) . Since the experimental FBGs has an initial peak reflection wavelength at 1549.25nm, this wavelength is chosen to present theoretical results here. It will also be assumed that a 3cm FBG will be centered inside of the 4cm trapezoidal slab and at the edge of the approximately acute Saccharin quadrilateral slab. As shown in this chapter, having a large linear chirping increases the spectral width of the reflected signal greatly and boosts its optical power moderately up to a upper limit. This can be easily understood by considering several non-uniform FBGs, each with a large difference in the period of each individual grating. The reflection spectra for each will not overlap with the other FBGs. Analyzing each FBG with the method in chapter 3, one will find a low peak power reflectance. However, the total reflected power (area under the spectrum) increases with linear chirping (see Figure 4-10). Thus, placing the FBG in an area with a large linear-like chirp is beneficial for power readings since a lower applied external magnetic field will have the low strain and power, but larger fields will create a high strain and power. The sensor sensitivity is controled by the chirp parameter, e.g. α_p, that enable the tuning of sensor performance by the composite geometry. Figure 4-11 shows the change in grating period for different sensors induced by non-uniform magnetization distributions under various applied external fields for an effective refractive index (n_{eff}) of 1.45, and a magnetostriction coefficient (ϵ_s) of 642ppm, as given in Eq. (4.84). Obviously, the approximately acute Saccharin quadrilateral slab maintains the increasing trend of the grating period and hence, generates higher frequency chirp. That means the formation of a chirped FBG. What is remarkable is that each period of the chirped FBG varies by the

same percentage as temperature changes, i.e. the shift of whole spectrum but maintaining the shape and the bandwidth of the spectrum. The property of the chirped FBG enable temperature independent sensing.

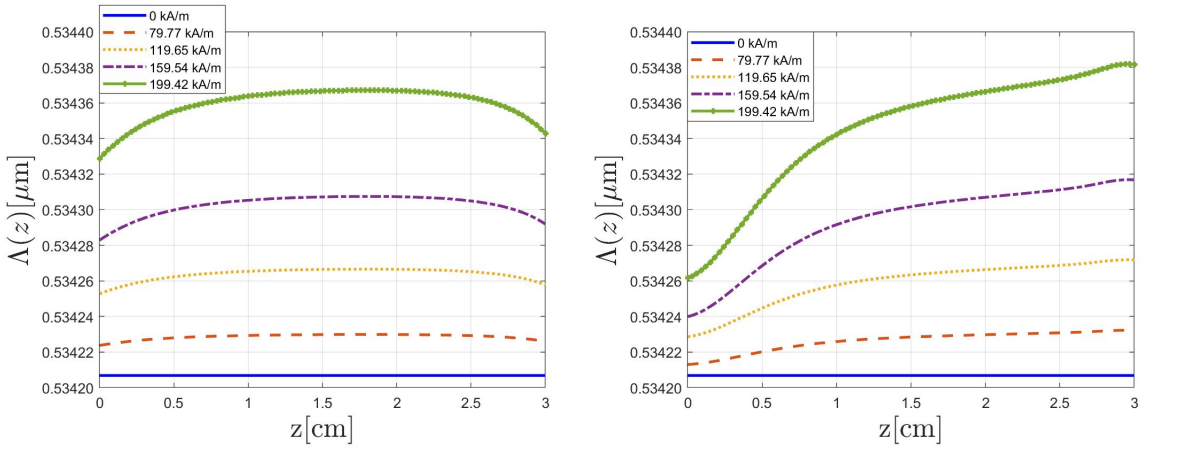

(a) Trapezoidal Slab **(b)** Approximately Acute Saccharin Quadrilateral Slab

Figure 4-11: Theoretical Estimation of Magnetostrictive Effect on Grating Period as a Function of z under Various External Magnetic Fields

Again, the refractive index perturbation in Eq. (4.76) introduced $\Lambda(z)$ in the beginning of this subsection that enables the consideration the tuning of the chirping factor with external magnetic fields. Figure 4-12 shows the spectrum change for different applied fields by using Eq. (4.75) for the same δn_{eff}, effective refractive index, and magnetostriction coefficient used previously ($n_{eff} = 1.45$, ϵ_s =642ppm).

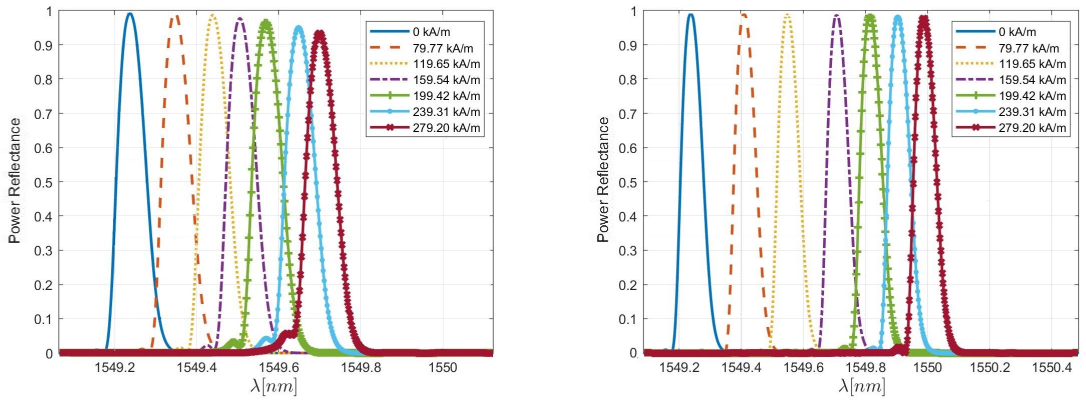

(a) Trapezoidal Slab **(b)** Approximately Acute Saccharin Quadrilateral Slab

Figure 4-12: Theoretical Reflection Spectra under Various External Magnetic Fields

Total Power

By integrating over the total spectrum, the reflected power may be calculated. As shown by Figure 4-12, it appears that the peak power reflection is getting lower, but the spread of the reflected spectrum in increasing. It is to be noted that the FBG that was modeled has a small chirping on the left side of the reflected spectrum which becomes very relevant as external magnetic fields are applied. Figure 4-13 shows the reflected power as the external field is varied using the same parameters used for the strain and spectra plots. The figure further confirms the increasing trend of the return power with the applied fields and shows the saturation in the return power under high external fields.

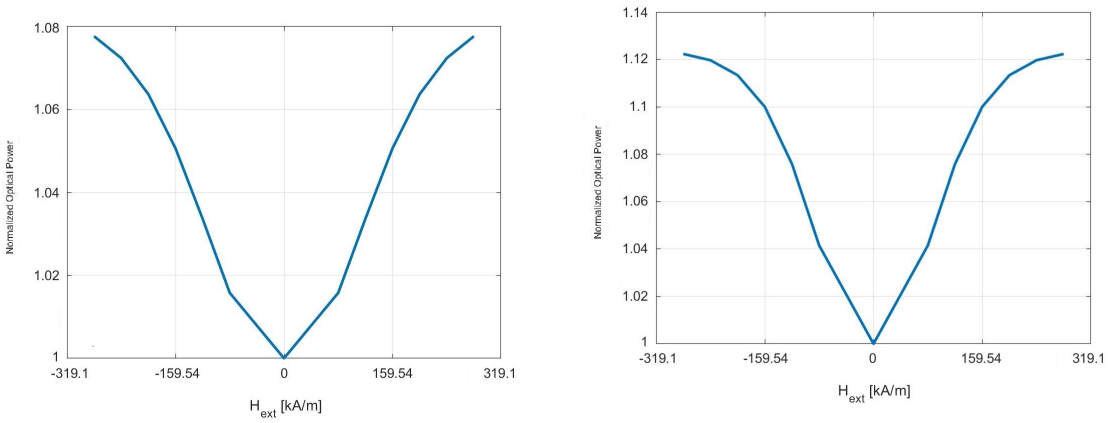

(a) Trapezoidal Slab

(b) Approximately Acute Saccharin Quadrilateral Slab

Figure 4-13: Theoretical Reflected Optical Power as a Function of the External Magnetic Field

THIS PAGE INTENTIONALLY LEFT BLANK

Chapter 5

Experimental Results

5.1 Introduction

In Chapter 4, the modeling of the internal field inside magnetostrictive composite slabs in two different geometries and the optical response of an FBG to magnetostrictive strain were discussed. In this chapter, the actual fabrication of magnetostrictive slabs and the embedment of an FBG to each slab as described. The combination of these components constitute a device known as magnetic field sensor. As mentioned in Chapter 1, this sensor will be instrumental for current fault detection in a power system. Its applications can be extended to metering and integrated with smart grids if its performance can be enhanced such as wider dynamic range and higher sensitivity. The sensor under consideration has potentials for these fronts. Before reaching these goals, proof-of-concept experiments need to be performed to characterize the sensor. Here, setup for these experiments is described, results are presented and their implications are elaborated.

5.2 Fabrication of Magnetostrictive Slabs

A rectangular aluminum slab was used a negative for creating a silicon mold for the fabrication of composite slabs as shown in Figure 5-1. After the silicon rubber was cured inside a cylindrical chamber with the negative, the negative was removed from the chamber and a mold was formed. The silicon mold was used to encase the Terfenol-D/epoxy composite while curing with an FBG centered along the axis of the cylindrical chamber. The magnetostrictive body was a composite of Terfenol-D particles (200-300μm) and an epoxy resin/hardener (Super Sap 100) from Entropy. The mixing ratio of the resin was 2:1. The resin was measured with a Gemini-20 scale to ensure the Terfenol-D to epoxy ratio of 1:3 in volume.

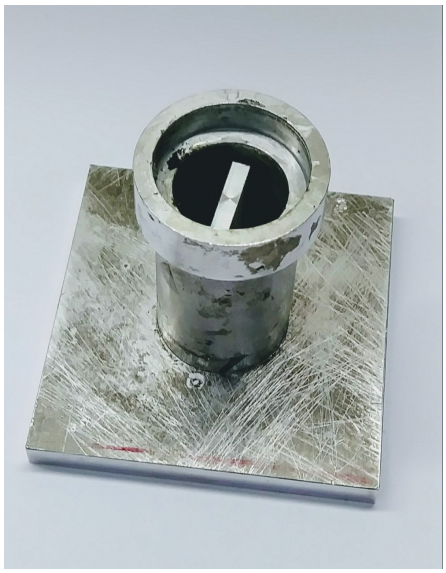

(a) Negative for Silicon Mold

(b) Mold for Shaping Particle-Epoxy Slurry into Rectangular Slab

Figure 5-1: Production of Mold

The resin was mixed with the hardener for approximately three minutes and then was placed in a vacuum chamber for five minutes to purge any air pockets. From here, the Terfenol-D was added to the resin and mixed for five minutes. Then the whole mixture was placed in the vacuum chamber again for another five minutes. These steps are illustrated

in Figure 5-2.

(a) Terfenol-D/Epoxy Composite

(b) Composite with FBG inside the Mold

Figure 5-2: Fabrication of Magnetostrictive Composite with an Embedded FBG

5.3 Attaching of Fiber Bragg Grating

Two 3cm FBG from O/E Land Inc. were used. The first FBG which was used for sample one had a linewidth of 0.1nm and a peak wavelength of 1549.35nm. The FBG in sample two had a linewidth of 0.095nm and a peak wavelength of 1549.24nm.The first FBG was placed through the center of a silicon mold for sample one and then the second FBG was positioned at the end of the mold for the second sample. The placement of FBG in the second sample ensures the FBG coupled to the appropriate strain distribution. Then the mixture was poured in the mold very slowly to ensure that no air pockets introduced by pouring. The curing mixture inside the mold with upper and lower openings was enclosed by a cylindrical chamber. The FBG was laced through openings at the top and bottom.

To ensure the FBG was centered inside of the sample along the longitudinal direction (the axis of the cylindrical chamber), the top hole was used as an anchoring point. The downward pointing end of the fiber was attached with a weight so that there was constant tension. The sample was then placed in a magnetic field oriented along the z-direction. The sample then cured for seven days and was removed and tested to check for initial changes in the reflected spectrum. The schematic in Figure 5-3 shows the experimental setup for making a rectangular Terfenol-D/epoxy slab with an embedded FBG.

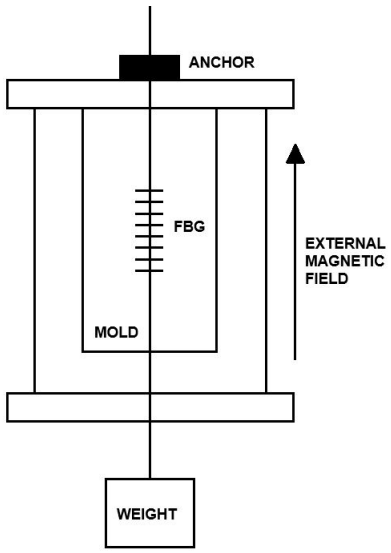

Figure 5-3: Rectangular Terfenol-D/Epoxy Slab Fabrication Process

For maintaining the FBG taut during the curing process, the appropriate weight was experimented and was found that an initial mass of 30 grams would break the FBG. Owing to this observation, mass was progressively added over 5 minute intervals. Since the pure epoxy is transparent and easy for checking conditions of the embedded object, it was used to make multiple 100% epoxy slabs for tests of the tension adjustment. A bare fiber was used with a initial mass of 10 grams. Weight was added in 5 grams increment for every 5 minutes until a final mass of 30 grams was reached. This process resulted in a centered fiber inside the pure epoxy slab and the same methodology was adopted for the fabrication

of the actual Terfenol-D/epoxy slab. After curing, the rectangular slab was then shaped roughly to the geometry of interest by a rotatory tool with a cutting wheel and fine-tuned by a sanding method with a grinding stone.

The composite was then placed in between a pair of rare earth magnets while curing to align the large particles of Terfenol-D. After the curing process, the composite was extracted from the silicon mold and ready to be shaped to desired geometries (see Figure 5-4). The composites were then cut to the desired geometries - a trapezoidal slab and an approximately acute Saccheri quadrilateral slab to finalize the fabrication of sensors, as shown in Figure 5-5. For the trapezoidal slab, the measured dimensions were $a = 5.24mm$, $b = 10.22mm$, $c = 3.18mm$, and $L = 39.82mm$ and the mass of Terfenol-D particles was estimated to be 0.647g . For the approximately acute Saccheri quadrilateral slab, the measured dimensions were $a = 6.3mm$, $b = 14.97mm$, $c = 3.18mm$, $L = 40.21mm$, and $L' = 28.05mm$ and the mass of Terfenol-D particles was estimated to be 0.976g . After initial curing of the composites for a week, and cutting to the correct geometry to form the sensors, they were set aside and cured for an additional 4 weeks. The additional curing was an appropriate action since the curing process is a very long, continuous process.

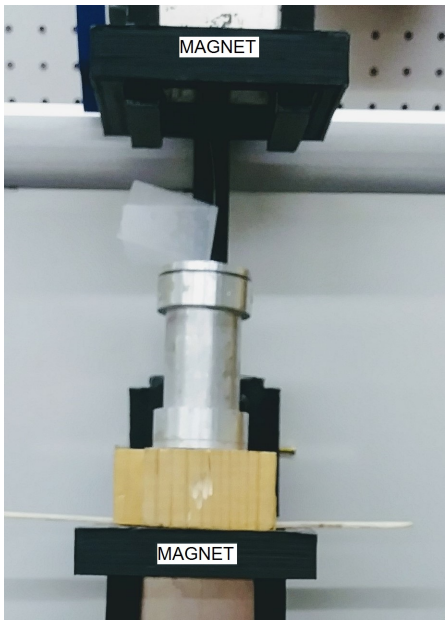

(a) Curing under Magnetic Field from a Pair of Rare Earth Magnets

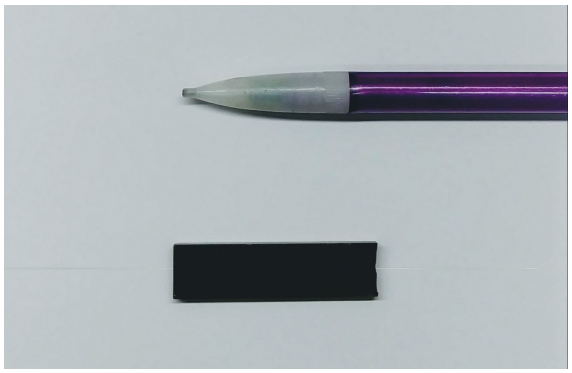

(b) Composite After Extraction

Figure 5-4: Curing and Extraction of Composites

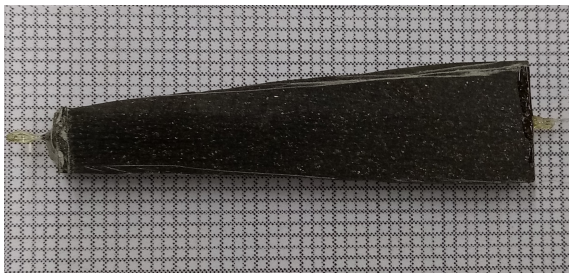

(a) Trapezoidal Slab

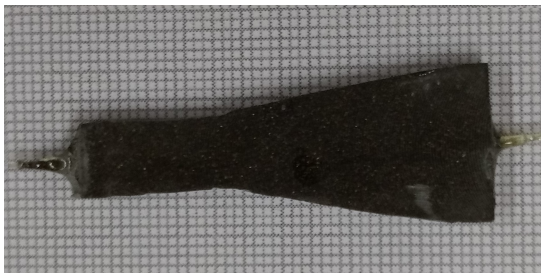

(b) Approximately Acute Saccheri Quadrilateral Slab

Figure 5-5: Sensors in Various Geometries

5.4 Optical Setup

Here, the procedure for the evaluation of a sensor or device under test (DUT) is briefly described. The optical source for the characterization of DUT was an Exalos EXS 1520-2111 SLED with a peak wavelength of 1550nm and a bandwidth of 63nm. The source was connected to an isolator to eliminate feedback. After this point, an optical circulator was used to route the input light from port 1 to port 2 toward the FBG that reflected a return

signal exiting the circulator through port 3. Then a directional coupler was used to split one half of the reflected light from port 3 to an optical spectrum analyzer (ThorLabs OSA 202). The other half of the light went to an optical power detector (ThorLabs DET01CFC InGaAs Detector) which delivered its photocurrent to a load resistor valued $33k\Omega$. The load resistor converted the photocurrent into a voltage that is proportional to the optical power and can be easily measured by a data acquisition (DAQ) system or a voltage meter. The power and spectral measurements were automated by a personal computer (PC) controled by a LabView program. Figure 5-6 shows the optical schematic.

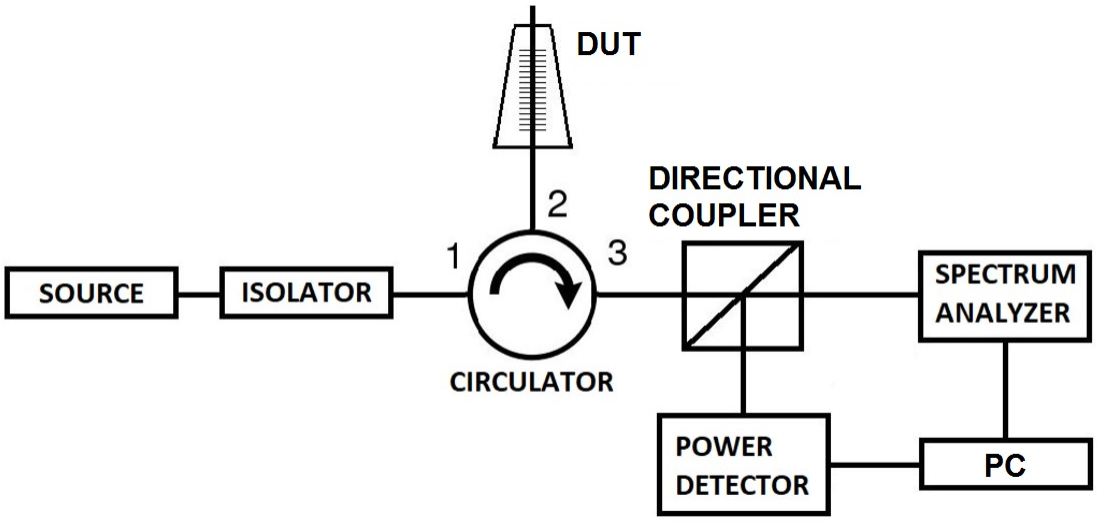

Figure 5-6: Optical Setup

Each DUT was individually tested under various magnetic fields generated by an electromagnet (Varian model V4005) and recorded with a Gauss meter (F.W. Bell 5180 Gauss/Tesla Meter). The field was varied from 0 Gauss to 3500 Gauss (0 kA/m to 279.195 kA/m), then back to 0 Gauss by increments of 500 Gauss (39.885 kA/m) . The polarity of the magnet was then switched and was cycled through 0 Gauss to -3500 Gauss, and then back down to 0 Gauss. As the magnetic field varying, optical power and reflectance spectra were measured with the optical setup in Figure 5-6. The corresponding test environment is shown in Figure 5-7. With the collected data, the spectral shift and variation of DUT

signal with the magnetic field were observed. Each DUT was tested multiple times for which a very small hysteresis was observed. Along with this, the overall shape of the power reflectance started to resemble the theoretical power after only one test cycle of applied magnetic fields([-3500G, 3500G]). The initial hysteresis shows that there is some memory associated with the initial testing of the samples. This would mean calibration of the sensor is necessary, particularly the properties of composites varying from batch to batch.

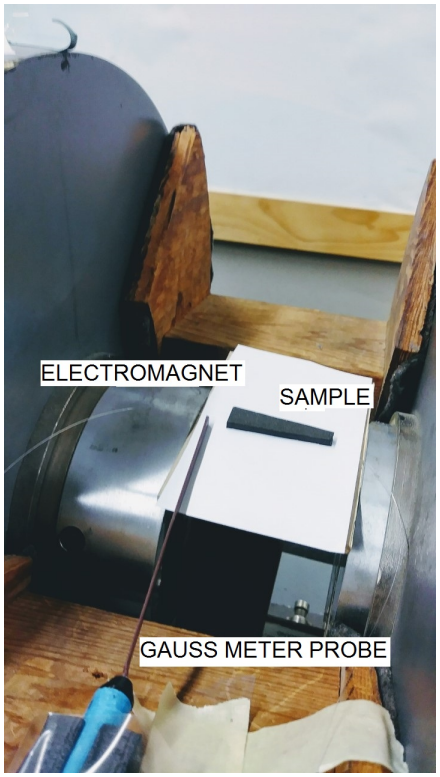

(a) DUT under Field from Electromagnet with a Gauss Meter Monitoring the Field

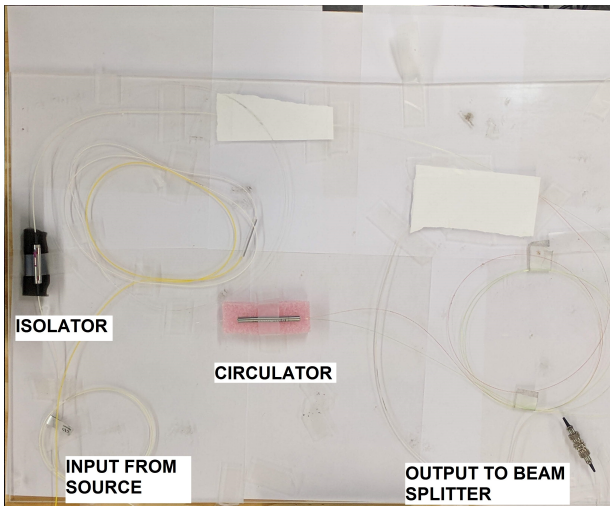

(b) Optical Setup

Figure 5-7: Testing Environment

5.5 Spectral Shift

A spectral shift has the possibility to occur from three parameters - compression from the curing process, thermal expansion of the magnetostrictive composites, and the applied

magnetic field which induced strain onto the samples. Minimizing the changes in spectral shape from the initial curing enables a magnetic field sensor to have maximum sensitivity and operating range. Figure 5-8 shows the spectral shifts of the FBGs caused by the curing process before the samples were cut to desired shapes. This process has been experimentally optimized with a procedure for adjusting tension by adding different weights as shown in Figure 5-3. Figure 5-9 shows the experimental data for the effect of thermal expansion effects on the sensors. Each sensor was placed inside an oven set to $70°C$ and left to be idle for approximately 15 minutes to ensure uniform heating of the sample. This preliminary test demonstrates that the each sensor maintains its spectral shape as the temperature changes.

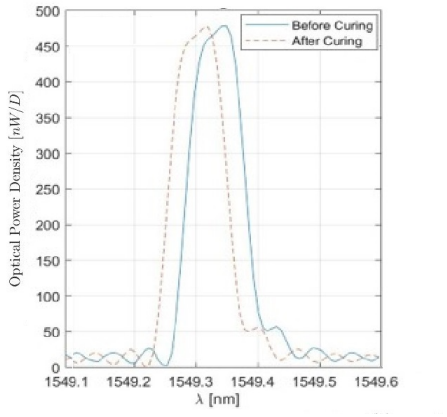

(a) First FBG with a Rectangular Slab

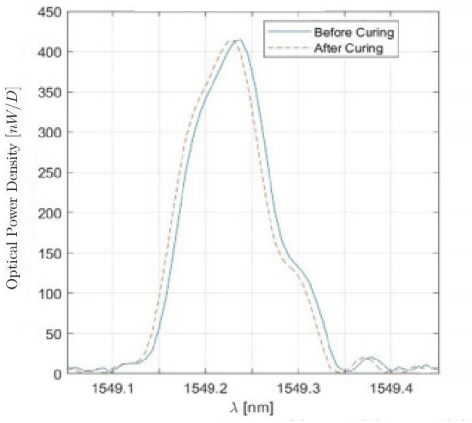

(b) Second FBG with a Rectangular Slab

Figure 5-8: Spectral Shift From Curing

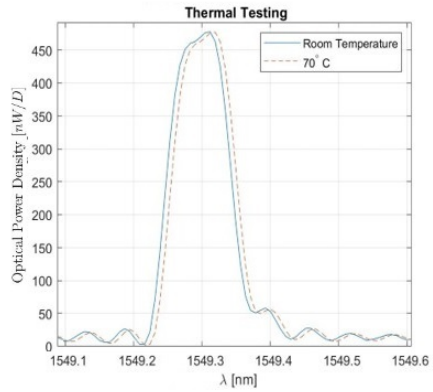

(a) Trapezoidal Slab

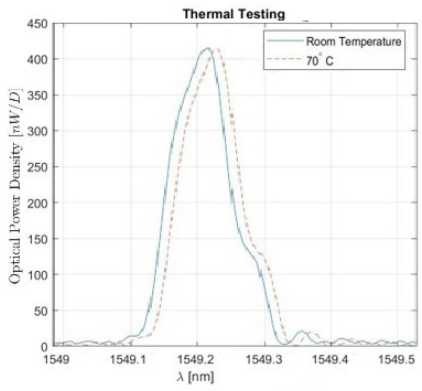

(b) Approximately Acute Saccheri Quadrilateral Slab

Figure 5-9: Spectral Shift From Thermal Testing

Figure 5-10 shows the recorded data on the spectral shift for the sensor due to an applied magnetic field. Four tests are initially used to examine the optical properties of the sensor, for which the spectral shift is presented for the fourth test. The shift of peak wavelength for no applied magnetic field to maximum tested magnetic field has a range of 0.38nm compared to the theoretical spectrum range of 0.40nm. The initial chirp of the FBG is shown to be changed significantly due to the spread of the linewidth as the applied magnetic field increases. The measurement for the spectrum was taken in optical power density $[nW/D]$, where D is the unit wavelength which was 0.1nm. The unit wavelength is based on a fixed wavelength band.

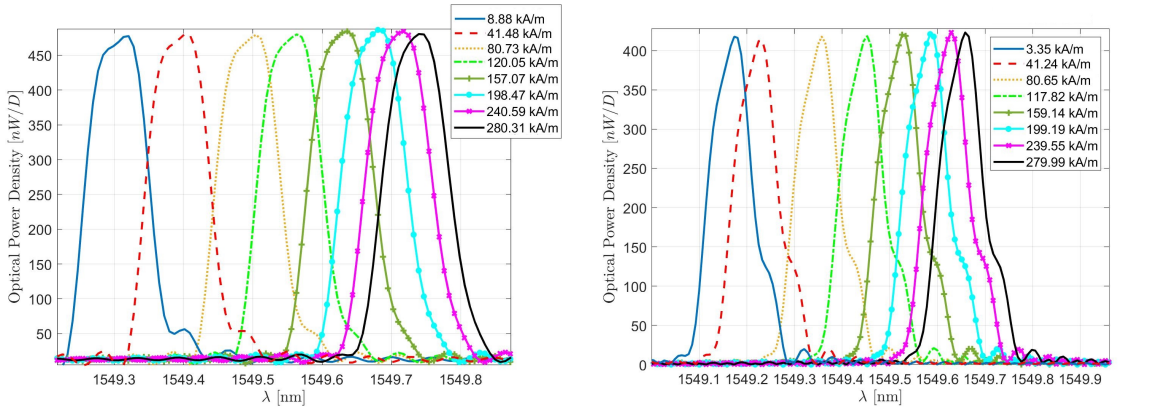

(a) Trapezoidal Slab **(b)** Approximately Acute Saccheri Quadrilateral Slab

Figure 5-10: Experimental Spectral Shift

5.6 Optical Power versus Magnetic Field

For purposes of comparing with theoretical predictions, the optical power was normalized without respect to the value at zero magnetic field. Direct measurements of the optical power were taken with two different photodetectors. The first being the ThorLabs detector and the second being a NEC NR7800 photodetector. The purpose of two detectors was to verify the independence of the detector on the optical power measurements. Figure 5-11 and Figure 5-12 show the first detector while Figure 5-13 and Figure 5-14 show the results

from the second detector. From observing the following figures, it can be seen that Test 1 differs from Test 4 significantly for both samples. For this research, after approximately 4 cycles, the experimental results resemble the shape of the theoretical predictions. These tests were performed back to back and one can observe that the initial test (test 1) is relatively different from the other tests. The ratio of the maximum normalized optical power from experiment to that from theory is 74% and the shape is consistent for the same comparison . The maximum power for the trapezoidal slab was 89 nW. The power was recorded from the Throlabs detector which was connected to the DAQ system and for the approximately acute Saccheri quadrilateral slab was 94 nW. The optical power was recorded by photodetectors which are photodiodes operating at the photoconductive regime. As an incident light (a flow of photons) is absorbed by the semiconductive material inside the photodiode, the photodetector outputs a photocurrent (a flow of electrons) proportional to the absorbed optical power and is converted into a voltage across the load resistor in the photodetector circuit. This voltage signal is collected by the DAQ system in experiments. The detector output voltage should not be larger than approximately 75% of the supply voltage since the detector will be saturated when operating beyond this limit, i.e. outside the photoconductive regime. The load resistor that was used for all tests was $33k\Omega$. Test 1 and Test 2 were done with the NEC detector while Test 3 and Test 4 were done with the Thorlabs detector.

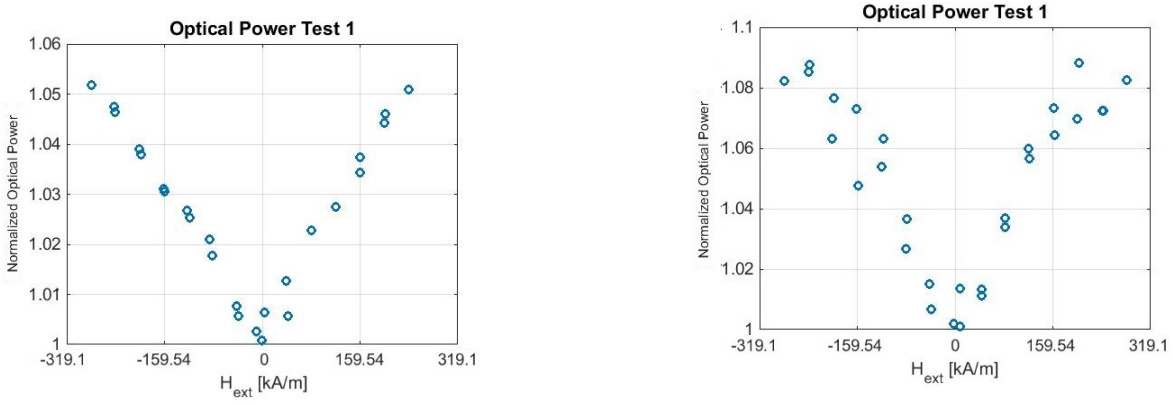

(a) Trapezoidal Slab

(b) Approximately Acute Saccheri Quadrilateral Slab

Figure 5-11: Experimental Reflected Power under Various External Magnetic Fields

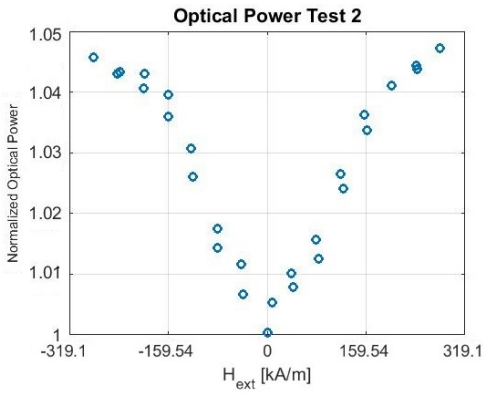

(a) Trapezoidal Slab

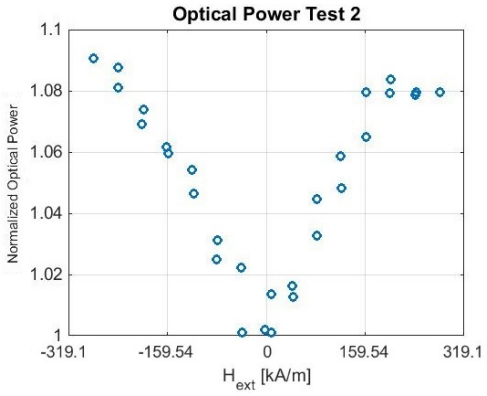

(b) Approximately Acute Saccheri Quadrilateral Slab

Figure 5-12: Experimental Reflected Power under Various External Magnetic Field

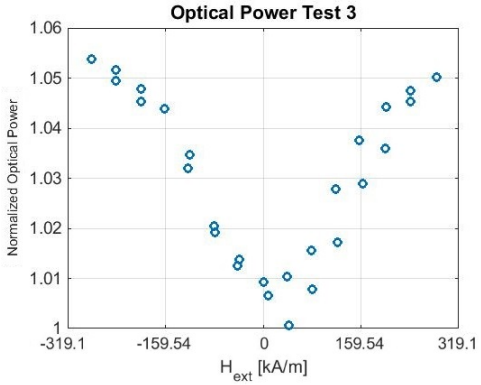

(a) Trapezoidal Slab

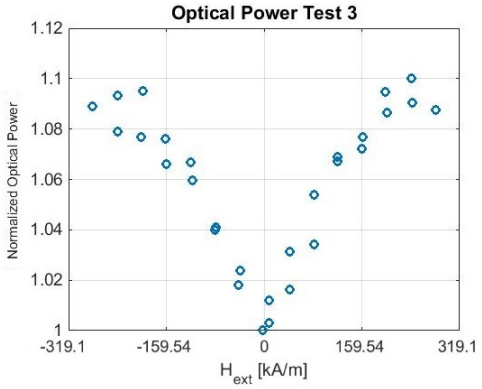

(b) Approximately Acute Saccheri Quadrilateral Slab

Figure 5-13: Experimental Reflected Power under Various External Magnetic Field

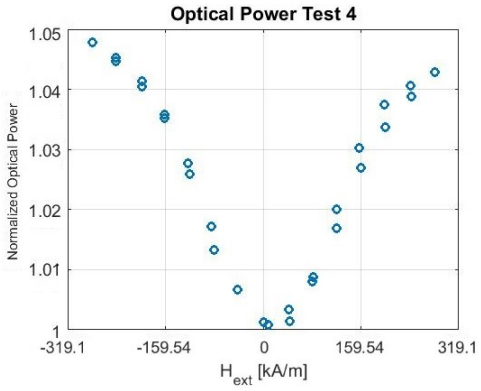

(a) Trapezoidal Slab

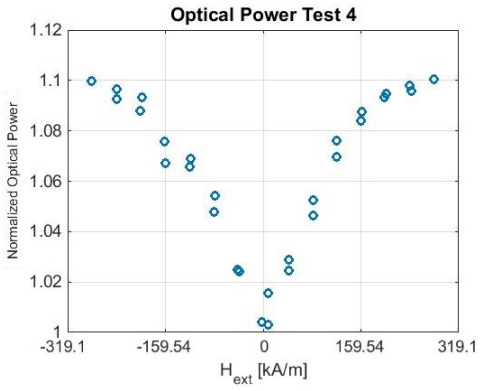

(b) Approximately Acute Saccheri Quadrilateral Slab

Figure 5-14: Experimental Reflected Power under Various External Magnetic Field

5.7 Estimation of Magnetostriction Coefficients from Data

By computing ratio the shift in peak wavelength $\Delta\lambda_p(H_{ext})$ and the peak wavelength under zero magnetic field applied λ_{p0}, it is possible to determine the change in the length of the FBG ΔL or strain on the sensor $\epsilon(H_{ext}) = \Delta L/L$ for external applied fields by the relation

$$\frac{\Delta\lambda_p(H_{ext})}{\lambda_{p0}} = \frac{N\Delta\Lambda(H_{ext})}{N\Lambda_0} = \frac{\Delta L(H_{ext})}{L} \tag{5.1}$$

where N is the number of grating periods. Figure 5-15 presents the data for the ratio $\frac{\Delta L}{L}$ for both experimental tests. The quadratic relation to find the magnetostrictive coefficient is expressed as $\frac{\Delta L}{L} = \frac{3}{2}\epsilon_s\frac{M^2}{M_s^2}$. The magnetization (M) can be approximated to be $\chi_m H_{int}(z)$ for which an average of the internal field may be taken such that $\frac{\Delta L}{L} = \frac{3}{2}\epsilon_s\frac{(\chi_m H_{int,avg})^2}{M_s^2}$. ϵ_s is the magnetostriction coefficient and M_s is the saturation magnetization which can be assumed to be very close of that to monolithic Terfenol-D. Solving for ϵ_s, the magnetostriction coefficient for the sensor with the trapezoidal slab was approximately 420ppm and for the sensor with the approximately acute Saccheri quadrilateral slab was approximately 560ppm. The simulation results with the updated magnetostriction constants are shown in Figure 5-16 and Figure 5-17.

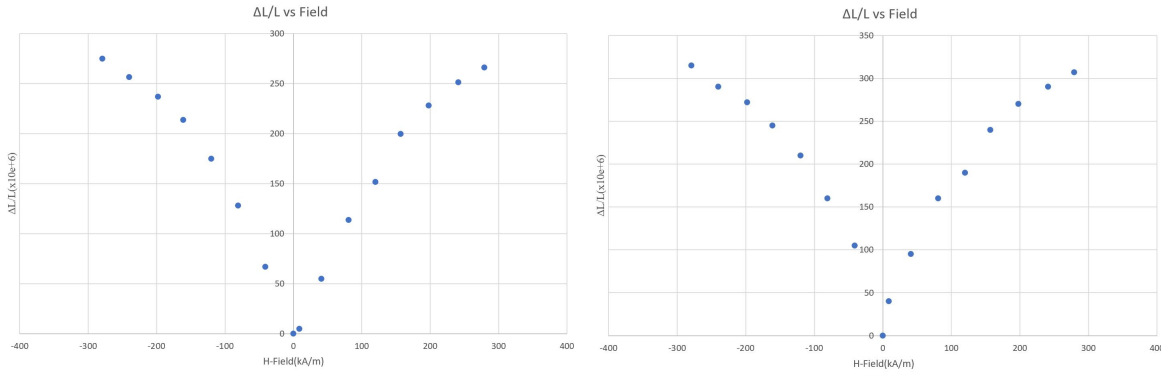

(a) Trapezoidal Slab **(b)** Approximately Acute Saccheri Quadrilateral Slab

Figure 5-15: Strain vs Applied Magnetic Field

By substituting this updated magnetostriction coefficient in, a better comparison between

the theoretical and experimental results can be obtained for the spectral shift and reflected optical power.

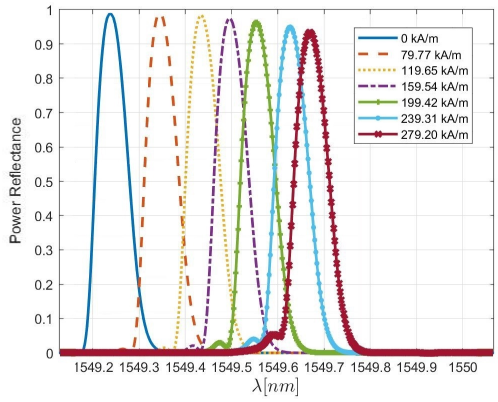

(a) Trapezoidal Slab

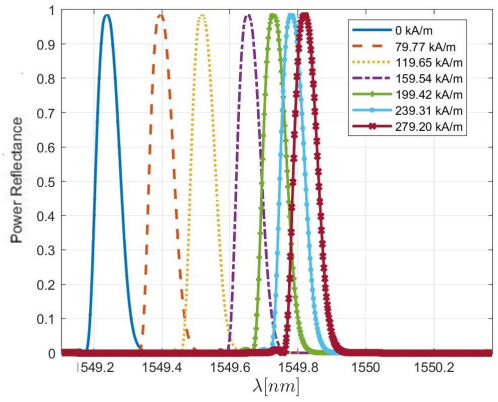

(b) Approximately Acute Saccheri Quadrilateral Slab

Figure 5-16: Theoretical power reflectance with Updated Magnetostriction Coefficients

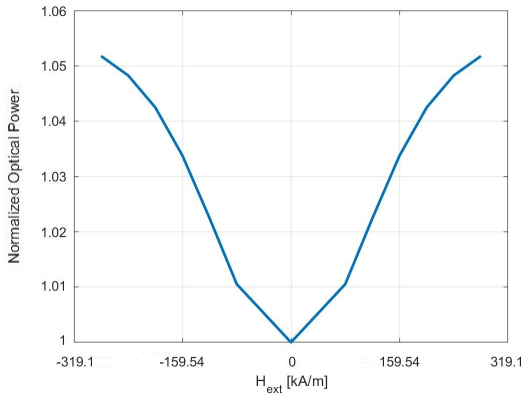

(a) Trapezoidal Slab

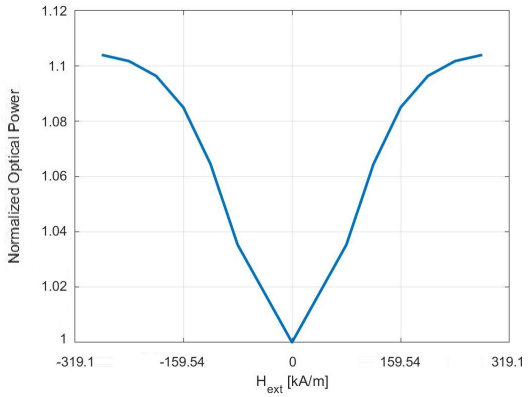

(b) Approximately Acute Saccheri Quadrilateral Slab

Figure 5-17: Theoretical power reflectance with Updated Magnetostriction Coefficients

Additionally, plotting the RMS linewidth ($(\Delta\lambda)_{RMS}$) against the magnetic field will be able to show if there is saturation for the strain. Figure 5-18 shows the data for both sensors for which it can be observed that the linewidth follows a linear like relation with the applied field. This shows that the material is not saturated and that the upper limit of the

sensor has not yet been reached. Thus higher magnetic fields are able to be measured. The saturation effect is mostly caused by the dropping of reflected power as linewidth increases.

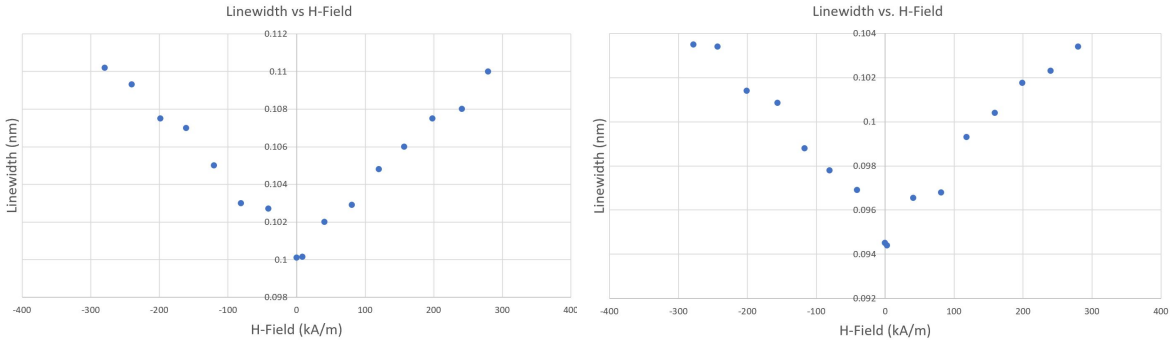

(a) Trapezoidal Slab **(b)** Approximately Acute Saccheri Quadrilateral Slab

Figure 5-18: Variation of Linewidth with External Magnetic Field

THIS PAGE INTENTIONALLY LEFT BLANK

Chapter 6

Conclusion

6.1 Conclusion

This thesis presented that theoretical modeling of the geometrically dependent magnetic field inside two quasi-two-dimensional magnetostrictive slabs, particularly trapezoidal and approximately acute Saccheri quadrilateral shapes. The internal magnetic field was coupled to an FBG through magnetostrictive strain which modified the FBG in terms of both the peak wavelength and bandwidth of its reflection spectra. Before the modeling of an FBG was discussed, a background on Terfenol-D was given along with the magnetostrictive strain characteristics as a function of magnetization and the wave transfer matrix method was introduced for modeling of the prominent resonances in the spectrum of an FBG with uniform period. The chapter on electromagnetic analysis for the FBG showed the actual technique being used to connect FBG response to magnetostrictive strain since it constitutes the best approach to model general perturbations, such as the magnetostrictive strain, in an FBG. With these models, the foundation was laid for modeling and predicting magnetic field sensing performance theoretically. Then the sensor fabrication and experimental procedure for characterizing two sensors based on the two quasi-two-dimensional magnetostrictive slabs were presented along with experimental data that provided a proof of concept for the magnetic field sensor. Besides demonstrating a very well match with the theoretical results, these experiments confirm the control of sensor sensitivity with the geometry of the mag-

netostrictive composite slab..

The intended application for the field sensor under investigation was in constructing FOCSs that form a sensing network for fault detection and location in a power grid. This design of FOCS serves as a more sustainable and effective in current sensing since small amount of magnetostrictive material is used in composite and the use of the frequency chirping in an FBG to infer magnetostrictive strain mitigate the averse effect of thermal expansion. Furthermore, the use of the frequency chirping enables the linking of optical power measurements to the external magnetic field and reduces the cost in signal processing. With the ability of sensitivity control, the FOCS under investigation has potential in serving at various current ranges and extending its dynamic range.

In summary, two magnetostrictive composite slabs with an embedded FBG have been fabricated and demonstrated repeatable and consistent performance with the theory. The spectral outputs of the sensors were almost linearly proportional to the external magnetic field in terms of their changes in spectral width and peak wavelength. The closely matched experimental and theoretical results verified the effectiveness of the fabrication procedure and reliability of the theoretical model that was critical for optimization of the sensor.

6.2 Further Research

More thermal testing will be required to demonstrate temperature independent sensing under various levels of the external magnetic field. For sensor optimization, different composite geometries will be designed and modeled. Before investigating more complicated geometries, various combinations of FBG length and parameters of approximately acute Saccheri quadrilateral should be considered in order to determine the minimum detectable magnetic field and maximum sensitivity under the best configuration. They will be verified first with COMSOL simulations and then confirmed by sensor fabrication and experiments. The optimized sensor will then be further examined with AC magnetic fields at different frequencies. The aim here is to search for the maximum operating frequency.

With thorough sensor characterization, the ultimate sensitivity and dynamic range of the optimized sensor should be determined. Based on this knowledge, applications of FOCSs for their uses in sensing networks for detecting current faults at various ranges should be investigated. Other applications, such as optical filters with tunable frequency and bandwidth and optical encryption, may be within the horizon.

THIS PAGE INTENTIONALLY LEFT BLANK

Bibliography

[1] K. Bohnert, A. Frank, L. Yang, G. M. Mueller, M. Lenner, T. Roininen, B. Guelenaltin, P. Gabus, S. V. Marchese, and A. Vujanic, "Fiber-Optic Current Sensor in 420 kV Circuit Breaker," in Conference on Lasers and Electro-Optics, OSA Technical Digest (online) (Optical Society of America, 2016), paper AW1J.2.

[2] M. M. Werneck and A. C. S. Abrantes, "Fiber-optic-based current and voltage measuring system for high-voltage distribution lines," IEEE trans. Power Delivery, vol. 19, pp. 947– 951, 2004.

[3] Chiu T. Law, Kalu Bhattarai, David C. Yu, *Fiber-Optics-Based Fault Detection in Power Systems*. IEEE Transactions on Power Delivery, Vol. 23, 2008.

[4] Y. N. Ning, Z. P. Wang, A. W. Palmer, and K. T. V. Grattan, *Recent progress in optical current sensing techniques*. Review of Scientific Instruments 66, 3097 (1995).

[5] K. Bohnert, P. Gabus, J. Nehring, and H. Brandle, "Temperature and Vibration Insensitive Fiber-Optic Current Sensor," J. Lightwave Technol. 20, 267- (2002) .

[6] Amnon Yariv and Harry V. Winsor, Proposal for detection of magnetic fields through magnetostrictive perturbation of optical fibers, *Opt. Lett.,* 5(3): 87-89, 1980.

[7] J. Mora, A. Díez, J. L. Cruz, and M. V. Andres, A Magnetostrictive Sensor Interrogated by Fiber Gratings for DC-Current and Temperature Measurement, *IEEE Photon. Technol.* ,12(12): 1680-1682, 2000.

[8] B. Yi , C. B. Chu , K. S. Chiang, Temperature compensation for a fiber-Bragg-grating-based magnetostrictive sensor, *Microw Opt Technol Lett*, 36(2): 211–213, 2003.

[9] K. S. Chiang, et al.,"Temperature-compensated fiber-Bragg-grating-based magnetostrictive current sensor for dc and ac currents," *Opt. Eng.*, 42, 1906—1909, 2003).

[10] Satpathi, D., et al. Design of a Terfenol-D Based Fiber-Optic Current Transducer, *IEEE Sensors Journal*, 5(11): 1057–1065, 2005.

[11] M. Yang, J. Dai, C. Zhou, and D. Jiang, Optical fiber magnetic field sensors with TbDyFe magnetostrictive thin films as sensing materials, *Opt. Express*, 17(23): 20777-20782, 2009.

[12] S. M. Quintero, A. M. Braga, H. I.Weber, A. C. Bruno, and J. F. Araújo, A magnetostrictive composite-fiber Bragg Grating sensor, *Sensors* (Basel, Switzerland), 10(9), 8119–8128, 2010.

[13] Ki D. Oh, Anbo Wang, and Richard O. Claus, Fiber-optic extrinsic Fabry–Perot dc magnetic field sensor," *Opt. Lett.*, 29: 2115-2117, 2004.

[14] T. Yoshino, K. Kurosawa, K. Itoh and T. Ose, Fiber-Optic Fabry-Perot Interferometer and Its Sensor Applications, *IEEE Journal of Quantum Electronics*, 18(10): 1624-1633, 1982.

[15] L. Jin et al, An embedded FBG sensor for simultaneous measurement of stress and temperature, IEEE Photon. Technol. Lett., 18(1): 154-156, 2006.

[16] Isaak D Mayergoyz, *Handbook of giant magnetostrictive materials*. Elsevier, 1999.

[17] C Tannous and J Gieraltowski, *The Stoner-Wohlfarth model of ferromagnetism. European Journal of Physics*, 29(3):475, 2008.

[18] Ching Yin Lo, Siu Wing Or, and Helen Lai Wa Chan, *Large Magnetostriciton in Epoxy-Bonded Terfenold-D Continous-Fiber Composite with [112] Crystallographic Orientation. IEEE Transactions on Magnetics*, 42:10, 2006.

[19] T. A. Duenas, Carman GP, *Particle distribution study for low-volume fraction magnetostrictive composites. J. Appl Phys*, 90:2433–9, 2001.

[20] T. A. Duenas and G. P. Carman, *Large magnetostrictive response of Terfenol-D resin composites. Journal of Applied Physics*, 87:4696, 2000.

[21] Rani El-Hajjar, Chiu Tai Law, and Alessandro Pegroti, *Magnetostrictive polymer composites: Recent advances in materials, structures and properties. Progress in Materials Science*, 97:204-229, 2018.

[22] A. Saleh and M.C. Teich, *Fundamentals of Photonics*. John Wiley & Son, 1991.

[23] Anthony A. Tovar and Lee W. Casperson, *Generalized Sylvester Theorems for Periodic Applications in Matrix Optics. J. Opt. Soc. Am. A*, 12(3), 1995.

[24] David K. Cheng, *Field and Wave Electromagnetics*. Addison-Wesley, 1989.

[25] H. Kogelnik, *Theory of Optical Waveguides*. pages 7-88. Springer Berlin Heidelberg, Berline, Heidelberg, 1988.

[26] A. Snyder, Coupled-Mode Theory for Optical Fibers, textitJ.Opt. Soc. Am., 62(11): 1267-1277, 1972.

[27] R.Boyd, *Nonlinear Optics*. Academic Press, 2008.

[28] A.Othonos, Fiber Bragg gratings, *Rev. Sci. Instrum.,* 68(12): 4309-4341, 1997.

[29] Amni Yariv and Pocji Yeh, *Photonics: optical electronics in modern communications*. Oxford University, 2006.

[30] M. Prabhugoud and K. Peters, Modified Transfer Matrix Formulation for Bragg Grating Strain Sensors, *J. Lightwave Technol.,* 22(10): 2302-2309 (2004).

[31] Kenneth O. Hill and Gerald Meltz, *Fiber Bragg Grating Technology Fundamentals and Overview. Journal of Lightwave Technology*, Vol. 15, 1997.

[32] R.M Measures, *Smart Composites structures with embedded sensores. Composites Engineering*, 2(5-7):597-618, 1992.

[33] K. Peters, M. Struder, J. Botsis, A. Iocco, H. Limberger, and R. Salathe, *Embedded optical fiber Bragg grating sensor in a nonunioform strain field: measurements and simulations. Experimental Mechanics*, 41(1):19-28, 2001.